Spring 2021

Prediction of Residual Stress and Distortion in Laser Powder Bed Fusion Additive Manufacturing

Bhanuprakash Sairam Kosaraju

PREDICTION OF RESIDUAL STRESS AND DISTORTION IN LASER POWDER BED FUSION ADDITIVE MANUFACTURING

by

Bhanuprakash Sairam Kosaraju

Bachelor of Technology
Visvesvaraya Technological University, 2017

Submitted in Partial Fulfillment of the Requirements

For the Degree of Master of Science in

Mechanical Engineering

College of Engineering and Computing

University of South Carolina

2021

Accepted by:

Lang Yuan, Director of Thesis

Austin Downey, Reader

Nikolaos Vitzilaios, Reader

Tracey L. Weldon, Interim Vice Provost and Dean of the Graduate School

ACKNOWLEDGEMENTS

I would like to thank Dr. Lang Yuan for giving me this opportunity to work on this project and guiding me throughout the process of my research. For guiding me with the technical part and in building my network to grow in my academic pursuits. His contribution has been highly valuable. I would like to thank him for his support throughout my research. It was a very good learning experience for me to work with you as I got most of my practical training from you like working with different software and printing parts in the lab. I really appreciate your input as it helped me to build my confidence. On this same note I would like to thank Dr. Austin Downey and Dr. Nikolaos Vitzilaios for gracefully accepting to review my work and participating on the Thesis Defense committee. I am deeply thankful for your time and inputs.

ABSTRACT

Additive Manufacturing (AM) has its proven advantages to unlock the design space and manufacturing capabilities for complex geometries with lightweights. Distortion is one of the most common defects that occur in Laser Powder Bed Fusion Additive Manufacturing (LPBFAM), which is caused by the significant residual stress during the printing process. This can lead to numerous process iterations to achieve the requisite form and fit tolerances.

In this study, Finite Element (FE) model that utilizes the element birth approach was developed to predict the residual stress and distortion in the LPBFAM process. The methodology leverages a simplified approach where the detailed scanning pattern with motion of microscale melt is supplanted by slice-by-slice activation. In the model, each mesh layer (slice) consists of one or multiple actual build layers (actual powder thickness). The model successively activates each mesh layer one at a time with an activation time and calculated body heat flux corresponding to the real fabrication process. This multiple layer activation approach yields great computational efficiency while substantially capturing the transient physics of the process. A benchmark case published by NIST, which documented the detailed distortion profile for a bridge geometry, was simulated by this model. The predicted residual stress and distortion were compared against the published experimental data, where good agreement was achieved. In addition, the predictions were also compared with the AM Modeler, an embedded

commercial package for AM process modeling in Abaqus. The pros and cons for different methodology were discussed. To further utilize the developed FE model, a thin plate with multiple mini channels was predicted to understand its distortion during the printing process. Lastly, since the methodology is general and it can be applied to other materials systems and AM methods that employ similar fabrication procedure, the distortion in a dog-bone geometry with PLA plastic in Fused Filament Fabrication process was demonstrated to conclude this study.

This work sets a solid foundation to continuously develop a robust computational model to mitigate distortion through the optimization of scanning paths based on critical geometry features and the overall thermal characteristics during LPBFAM process. It will be a key component in a suite of numerical tools that enable virtually guided certification for LPBFAM process.

TABLE OF CONTENTS

ACKNOWLEDGEMENTS iii

ABSTRACT iv

LIST OF TABLES viii

LIST OF FIGURES ix

LIST OF ABBREVIATIONS xi

CHAPTER 1 INTRODUCTION 1

CHAPTER 2 LITERATURE REVIEW 4

2.1 ADDITIVE MANUFACTURING 4

2.2 CLASSIFICATION OF AM TECHNOLOGIES 4

2.3 RESIDUAL STRESS IN LPBF PROCESS 8

2.4 MODES OF HEAT TRANSFER 10

2.5 DEFECTS IN LPBF PROCESS 13

2.6 MITIGATING RESIDUAL STRESS AND DISTORTION 17

2.7 PREDICTION OF RESIDUAL STRESS 22

CHAPTER 3 MODELING METHODOLOGY 26

3.1.MODEL CHANGE METHOD (LAYER- WISE ACTIVATION): 26

3.2.PROGRESSIVE ELEMENT ACTIVATION METHOD: 37

CHAPTER 4 MODEL VALIDATION VIA BENCHMARK CASE 42

4.1 PART DEFLECTION: BENCHMARK NIST-AMB2018-01..... 43

4.2 STRESS PREDICTIONS..... 47

CHAPTER 5 APPLICATIONS..... 49

5.1 CHANNEL PLATE ANALYSIS 49

5.2 DOG-BONE..... 54

CHAPTER 6: CONCLUSION & FUTURE SCOPE 58

REFERENCES 60

LIST OF TABLES

Table 2.1: Classification of Additive Manufacturing Processes 5

Table 2.2: Parameters effecting printed part properties. 6

Table 3.1: Types of FEA simulation approaches 26

Table 3.2: Process parameters and simulation conditions 28

Table 4.1: Error ratio benchmark Vs model change, PEA 44

Table 5.1 General Material Properties 50

Table 5.2: Density Latent Heat, solidus and liquidous temperature 50

Table 5.3: Material properties of PLA [35] 55

LIST OF FIGURES

Figure 2. 1: Powder bed fusion additive manufacturing [3] 7

Figure 2. 2: Distortion caused in the part due to 10

residual stress in a part built by LPBF 10

Figure 2. 3: Modes of heat transfer [13] 11

Figure 2. 4: Layer delamination and cracking defects in PBF [7] 13

Figure 2. 5: Alternating scan pattern: 19

Figure 2.6: Effect of scanning strategy on residual stress 19

Figure 2.8: Inherent strain 22

Figure 3.1: Body heat flux [28] 27

Figure 3.2: Material properties of IN-625 [30] 29

Figure 3.3: Workflow model change 31

Figure 3.4: Part and substrate meshed 32

Figure 3.5: Substrate boundary condition 32

Figure 3.6: Steps: step-1(odd Steps) time periods 33

Figure: 3.7: Layer-wise partitioning 35

Figure 3.8: Layer wise activation 36

Figure 3.9: AM modelling plug-in 39

Figure 3.10: G-code material, laser 40

Figure 3.11: Elemental activation from event series data 41

Figure 4.1: 2-D model of bridge profile..... 42

Figure 4.2: 3-D model of bridge profile with substrate 43

Figure 4.3 Deflection comparison benchmark results Vs..... 44

model change prediction, PEA 44

Figure 4.4 Deflection profile in model change method (overall) 46

Figure 4.5: PEA method deflection 46

Figure 4.6: Stress profile - model change method 47

Figure 5.1: Plasticity 50

Figure5.2: Physical Model: Ears on rights and left U3=0 51

Figure5.3: Base nodes (U1=U2=U3=0)..... 51

Figure: 5.4: Central nodes (U3=0)..... 52

Figure 5.5: Deflection of Channel Plate 52

Figure 5.6 Stress profile a) Von Mises 53

Figure 5.7: 2D view of dog-bone profile in NATFAB. 54

Figure: 5.8 Fused filament fabrication [34] 54

Figure 5.9: NT11 Model change method..... 56

Figure 5.10: NT11 PEA method..... 56

Figure 5.11: Temperature Vs Time Model change, PEA methods..... 57

LIST OF ABBREVIATIONS

AM ..... ……Additive Manufacturing

ALM..... Additive Layer Manufacturing

DED.....Directed Energy Deposition

FEA .....Finite Elemental Analysis

LOF ..... ……Lack of Fusion

LPBFAM.....…Laser Powder Bed Fusion Additive Manufacturing

NDT..... ……. Non-Destructive Testing

PBF..... ……. Powder Bed Fusion

PEA ..... Progressive Elemental Activation

RP..... ……. Rapid Prototyping

RS..... ……...Residual Stress

SLM..... ……. Selective Laser Melting

CHAPTER 1 INTRODUCTION

Metal industrial products have been traditionally manufactured using various forms of casting and molding in combination with forming that can include forging, rolling, and extrusion processes. In most cases these methods are combined with machining using subtractive processes and then joining to produce a part or other product. Along with traditional and subtractive methods, powder-based processing methods have been used for part production especially for geometrically complex structures. Over decades, experience and analysis has been combined to formulate codes and standards as well as to mature various characterization, testing and evaluation methods that identify classes of defects, select alloys for applications, and assess their significance when incorporated into advanced computational models. There is now an increasingly diverse range of additive manufacturing (AM) process techniques that provide the ability to produce parts directly from computer-generated models with little to no additional material removal, without additional tooling required.

AM is a process of layer-by-layer addition of material of thin slices using different joining mechanisms, e.g. cohesive bonding, sintering, and melting obtain the intermediate or final design geometry of the part. AM process have been initiated for a quite long time ago since 1984 [1] but refinement in the quality of build is currently still ongoing and a topic of deep research in the scientific community. The aerospace, automotive and bio-medical industry has become increasingly interested in the potential use of AM methods to produce high-temperature, organic and stable components. Key

`drivers for this include the ability to produce complex net shape components without the same restrictions imposed by traditional machining and the ability to rapidly produce small batches of complex components without the prohibitive setup costs of traditional casting techniques [2].

Among all the AM process, laser powder bed fusion (LPBF) additive manufacturing is one of the most widely used technique to fabricate metallic components with fine feature resolutions. In this process, laser selectively melts ultra-thin layers of powder to form the desired geometry. However, due to extensive melting and solidification, defects like porosity, cracking and distortion are commonly observed in the final products. In order to achieve the desired dimensions and materials properties, significant process development time, typically based on trial-and-error methods, is required for novel designs that utilize the method's full potential, particularly for high value components. For this reason, it is necessary to develop new and to adapt current computational tools for the assessment of microstructural features and provide reliable detection and characterization of defects. Developing such tools with a good understanding of the mechanisms of defect formation like residual stress, distortion effects during the manufacturing process should enable AM methods to be more widely adopted with significantly reduced process development time for any introduction of new designs or new materials. It is also necessary to understand the significance of the various classes of defects on part functionality and life under the influence of operational stresses. When considering a components life cycle, it is desirable to optimize the manufacturing process with ideal scanning strategy and then plan monitoring and replacement of parts before they fail.

The development of computational tool to predict the residual stress and distortion in LPBFAM are core of this study. The thesis is organized in this following manner: Chapter 2 provides a comprehensive literature review starting with classification of AM technology, drawing attention mainly onto LPBF process, it identifies and talks about various defects during the LPBF, it specifically talks about RS, distortion and effect of scanning strategy on RS and distortion. It concludes with drawing focus over prediction and mitigation strategies. Chapter 3 describes in detail on Layer-Layer model change method and PEA method the two distinct methodologies in process of prediction of RS and distortion. It details on parameters and workflow that is to be considered for these processes. Chapter 4 validates the results of stress and displacement of Layer-wise model and PEA model with benchmark results provided by NIST 2018 AM benchmark results and finally, Chapter 5 concludes the current study and provides direction of future research.

CHAPTER 2 LITERATURE REVIEW

2.1 ADDITIVE MANUFACTURING

AM, which is generally also known as 3D printing, is the process of layer-by- layer addition of material of thin slices using different material binding processes [1] to obtain the final part as per the designed geometry in the three-dimensional CAD software, AM process eliminates the need for tooling, assembly compared to the conventional manufacturing processes.

2.2 CLASSIFICATION OF AM TECHNOLOGIES

The AM process are diversly classified based on the form of feedstock (Powder, Sheets or Wire) the type of power source (Laser, Electron Beam). All metal AM processes must consolidate the feedstock into a dense part. The consolidation may be achieved by melting or solid-state joining during the AM processes to achieve this. To discuss distinct classes of machines, the ASTM F42 Committee on Additive Manufacturing has issued a standard on process terminology [1]. Of the seven F42 standard categories, the following four pertain to metal AM:

Out of these various classifications for the sake of our research work, we focus on Laser Powder Bed Fusion, also commonly known as Selective Laser Melting process, and study the development of residual stress and distortion during the printing process.

Table 2.1: Classification of Additive Manufacturing Processes

Powder Bed Fusion (PBF)	Selective laser Melting (SLM)
	Electron Beam Melting (EBM)
Direct Energy Deposition (DED)	Laser vs. Electron beam
	Wire fed vs. Powder fed
Binder Jetting	Infiltration
	Consolidation
Sheet Lamination	Ultrasonic Additive Manufacturing (UAM)

2.2.1 POWDER-BASED ADDITIVE MANUFACTURING PROCESSES

LPBF and directed energy deposition (DED) are two AM processes where powders are the feedstock. In both these methods, the processing parameters and raw material characteristics influence the quality and mechanical properties of the as deposited parts. The physical mechanisms by which the various processing parameters and powder characteristics influence the parts microstructure, defect populations, and attending mechanical properties are topics of multiple ongoing research efforts across the AM community. While the mechanisms by which various process parameters influence defects and microstructure may not be completely known, several parameters associated with PBF and DED powder-based AM technologies have been correlated with defects and microstructure. These parameters include the quality of the powder feedstock and the power imparted by the heat source. Although there are more parameters that are common to PBF and DED than there are differences, the differences are important and will impact the thermal gradients of the molten pool and surrounding material. So the molten pool size, powder feed rate, and shielding gas flow are all critical process

parameters [3] . In the PBF method, pre-heating of the powder bed influences the solidification process and thermal gradient in the part. The following process parameters and material attributes that affect the final part properties are listed in Table 2.2.

Table 2.2: Parameters effecting printed part properties.

Process Parameters	**Powder Parameters**
Scanning rate (speed)	Grain Size
Heat Source energy (laser/electron beam)	Specific Heat
Scanning spot size (radius/ length)	Melting Temperature
Shielding gas flow rate	Thermal Conductivity
Bed Temperature	Absorptivity
Powder flow rate	Emissivity
Scanning hatching pattern	

The physical processes that occur during AM are complex and are just beginning to be fully understood and quantified [4]. Indeed, the particles not only move during the AM process, but that the fundamental physics of the process (e.g. metal vapor flow) are highly variable, and can create, effectively, vortexes which cause the powder to move. Once entrained in the liquid, the melt pool dynamics are equally complex, with Marangoni convection, evaporation, wetting, and capillarity playing strong roles (among many other operating physics). The liquid metal velocity is quite high, and results in features that resemble comet tails as melting particles leave molten material behind them as they move through the molten pool [4]. These physics present challenges in understanding and modelling AM processes, but it is expected that over the next three to five years, several

research groups will be able to contribute to the knowledgebase of the heat source/particle interactions. [3]

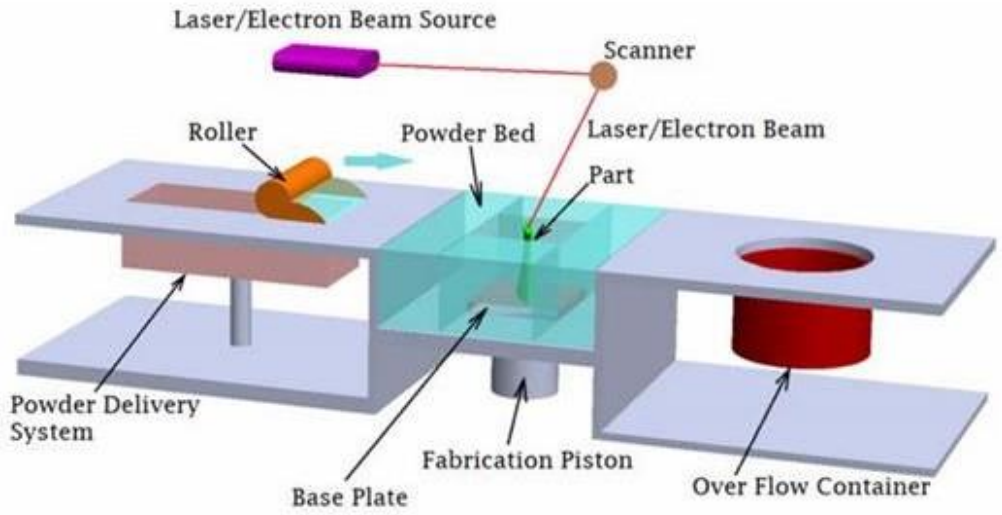

Figure 2. 1: Powder bed fusion additive manufacturing [3]

2.2.1.1 POWDER BED FUSION

Powder bed fusion (PBF) systems normally include a heat source, an automatic powder layering mechanism, a computer control system and related sensors and accessories. Such a system is shown in schematic form as Figure 2.1. LPBF is a specific application of PBF technology [3] with laser beam as the heat sources, it is a new kind of rapid prototyping (RP) technology. Its biggest advantage is the capability of fabricating. nearly 100 percent dense metallic parts, compared to other RP technology such as Stereolithography (SLA), Selective Laser Sintering (SLS), etc. SLM is layer-wise material addition technique that allows generating complex 3D parts by selectively melting successive layers of metal powder on top of each other, using thermal energy supplied by a focused and computer-controlled laser beam. It is widely used in the rapid direct manufacturing of mold parts and customized medical appliances in complex shape [6].

The LPBF process typically consist of a laser source, vacuum chamber filled with shielding gas (Argon), re-coater blade or roller, overflow chamber, powder bed and powder delivery chamber as shown in the Figure2.1. The movement of the laser source is operated by a computer based on the 3D CAD design of the part that is pre-loaded into it. The build chamber is a sealed work space filled with flow of shielding gas and mix of oxygen, in the build chamber the powder bed is at center of powder delivery system over the left and powder overflow chamber onto the right, initially the base plate is fixed in position over the fabrication piston and the top surface is coated with a thin slice of powder (SS316) by the movement of re-coater blade from powder delivery system (base position) which is filled with powder to the overflow chamber (intermediate position), then the laser begins the print of 1^{st} layer from the sliced file, now powder is again spread over the previous layer in each step of production using a roller or a blade, the roller comes back to the initial position from previous intermediate position and recoats the surface of the base plate with another layer of powder that is carried from the powder deliver chamber and once again rests at the intermediate position while laser prints the 2^{nd} layer. After each step of layering, the build platform lowers the part so the process can be repeated for subsequent layers till all the sliced layers are printed to form the required component. Laser sources typically utilize ans inert gas environment or gas shielding to prevent excessive oxidation. Typically, melting processes are faster than sintering, but require higher energy expenditure.

2.3 RESIDUAL STRESS IN LPBF PROCESS

Residual stress (RS) is common exhibited in metal AM materials and it can negatively impact mechanical properties and act as a driving force for changes in grain

structure and dimensional accuracy of the final product [7],[8]. The rapid heating-cooling thermal cycle of AM process, which is very similar to welding process, together with the large thermal gradient, results in residual stresses that are retained within a body when there are no external forces are acting on the body and it has reached equilibrium with its environment [9]. If this stress exceeds the local yield stress of material, warping or plastic deformation occurs. If this stress exceeds the local ultimate tensile strength of the material, cracking or other defects may occur. Macroscopic residual stresses can have a dramatic effect on the bulk behavior of AM parts, whereas the effects of microscopic residual stresses from precipitates or atomic dislocations are more localized[30].

Macroscopic residual stress can be thermally introduced in metal AM by (1) differential heating of the solid and (2) differential cooling during and after solidification. Residual stresses[31] are generally classified according to the scale at which they occur, Type I residual stresses: which vary over large distances, namely the dimensions of the part.

These macro stresses can result in large deformations of the part. Type II and Type III residual stresses: occur due to different phases in the material and due to dislocations at atomic scale, are not considered in this study[10], since they are of less importance for the geometrical dimensions. Moreover, the measurement resolution of most test methods is not small enough to measure type II and type III residual stresses.

Residual stress is a concern because it can negatively affect the mechanical properties of the fabricated parts or lead to geometrical distortions, it may also influence recrystallisation. Several techniques have been applied to measure residual stress in AM parts they can be categorized as either nondestructive or destructive; both categories have

benefits and drawbacks and tend to be application specific. The most used nondestructive methods are X-ray and neutron diffraction [11], which can provide near surface and volumetric residual stress measurements in crystalline materials, respectively.

To predict the residual stress during fabrication, different methods of finite element analysis (FEA) have been developed and are proven fast and reliable [12] (Benchmark model), offering leverage to optimize the design based on the results from the predictions. The magnitude of residual stress and the ways to reduce it are process dependent.

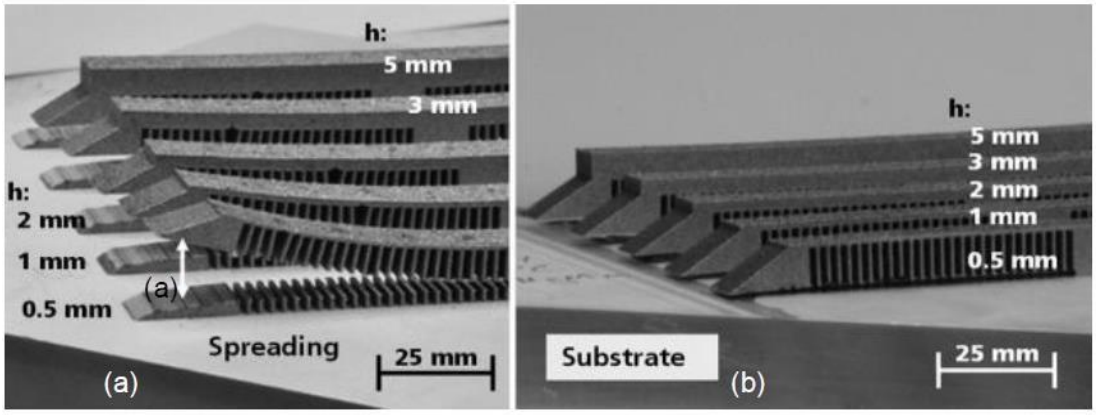

Figure 2. 2: Distortion caused in the part due to residual stress in a part built by LPBF a)No Preheating (b) Preheated to 200 °C [5]

2.4 MODES OF HEAT TRANSFER

Since the thermal cycle and thermal gradient drive the residual stress, it is important to understand how the modes of heat transfer differ between AM processes [7], [13]. After powder is melt, solidification determines the initial phase distribution and grain morphology of the metal deposit. The factors which determine the solidification kinetics are:

1. Heat Source

2. Speed, Power

3. Size Determines Melt Pool Geometry.

After solidification, thermal cycling and cool down path further determine the phase growth and grain growth. It is important to understand how the modes of heat transfer differ between AM processes. In LPBF processes transfer heat primarily through conduction to the substrate, conduction to the build material and convection to the shield gas [7].

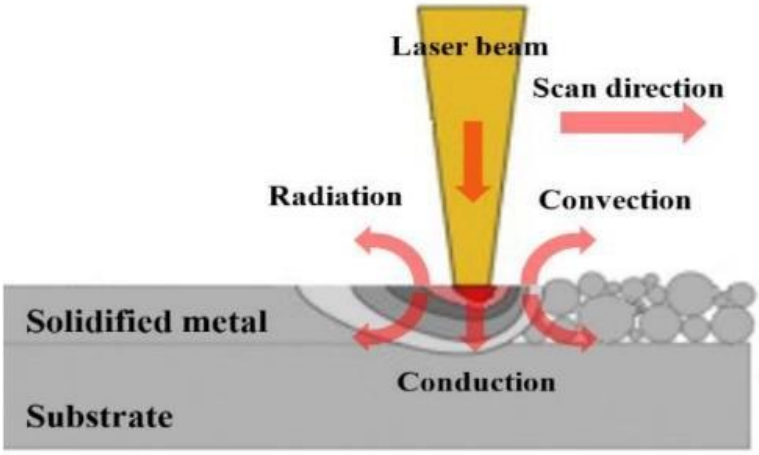

Figure 2. 3: Modes of heat transfer [13]

These modes of heat transfer are the same as those for welding. However, in LPBF processes, conduction may be inhibited by powder acting as a thermal insulator surrounding the part. Additionally, the fill gas in LPBF has a lower flow rate (argon gas consumption of 0·035–0·070 m^3/h). LPBF processes may use heaters to increase the temperature of the build envelope to 100–200°C. This is intended to reduce residual stress and warping but is not high enough to significantly impact the phase and grain structure of typical AM alloys. The mode of heat transfer can have important microscopic implications. For example, the depth of a melt pool is typically controlled by the

conduction of heat from the melt pool to material underneath. However, keyhole mode formation of porosity can occur when the depth is controlled by metal evaporation. Being able to transition between calculations on this microscopic scale and calculations of bulk heat transfer is important and is discussed later along with computational modelling of metal AM processes.

2.4.1 THERMAL ANALYSIS

The governing equation for heat transfer energy balance is written as [13]:

$$\rho Cp\, dT/dt = -\nabla \cdot q(r,t) + Q(r,t) \qquad (2.1)$$

where ρ is the material density, Cpis the temperature dependent specific heat capacity, T is the temperature, t is the time, Q is the volumetric internal heat generation rate, x is the relative reference coordinate, and q is the heat flux vector. The Fourier heat flux constitutive relation is: **Conduction (Part to Substrate)**

$$q = -k\nabla T \qquad (2.2)$$

where k is the temperature dependent thermal conductivity. Thermal radiation q(rad) is calculated using the Stefan-Boltzmann law: **Radiation. (melt pool to shielding gas)**

$$q(rad) = \varepsilon\sigma(Ts4 - T\infty 4) \qquad (2.3)$$

where ε is the surface emissivity, σ is the Stefan-Boltzmann constant, and Ts is the surface temperature of the workpiece. Newton's law of cooling calculates convective heat loss q(conv): **Convection (shielding gas & Part)**

$$q(conv) = h(Ts - T\infty) \qquad (2.4)$$

where h is the convective heat transfer coefficient. From the above Equations (2.1) – (2.4) the heat absorbed by the material during the melting, solidification and cooling

process can be calculated from the vector. Further this data is used by software like ABAQUS to interpolate the stress and part distortions caused by this thermal gradient.

2.5 DEFECTS IN LPBF PROCESS

The major defects in LPBF process can be due to Residual stresses and distortion [14]. The formation of defects is essentially dependent on process, temperature, and process parameters (laser power, layer thickness, porosity) [3], [7]. Cracking of the microstructure may occur during solidification or subsequent heating. Macroscopic cracks may relate to other defects, including porosity. Delamination leading to interlayer cracking is shown in Figure 2.4 If the process temperature is too high, a combination of melt pool size and surface tension may lead to swelling or melt balling. If processing conditions are tightly controlled, most of these defects can be avoided. Cracking of the microstructure is material dependent as well, and there may be some processing cases where cracking is unavoidable. There are different material-dependent mechanisms.

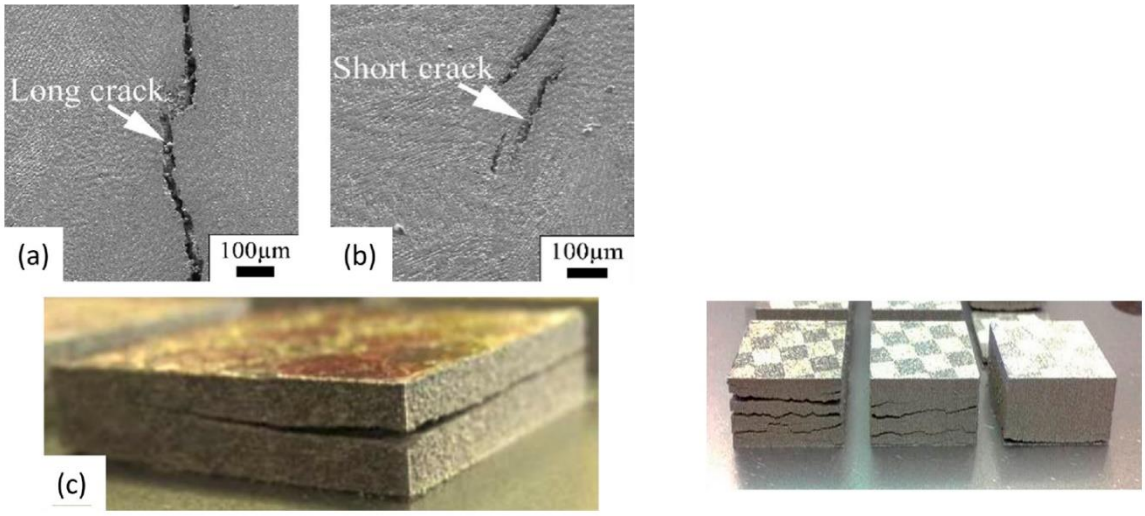

Figure 2. 4: Layer delamination and cracking defects in PBF [7]

because of which cracks are formed in the AM material [15]. Solidification cracking can occur for some materials if too much energy is applied, and this arises from the stress induced between solidified areas of the melt pool areas that are yet to solidify. This type of cracking is dependent upon the solidification nature of the material (dendritic, cellular, planar) and is typically caused by high strain on the melt pool or insufficient flow of liquid to inadequate supply or flow obstruction by solidified grains. Higher applied energy leads to higher thermal gradients, which can explain the larger thermal stress required for solidification cracking.

Influence of defects: The existence of defects can cause parts to have poor mechanical properties under certain loading conditions. It has been found that fatigue cracks are usually initiated from stress concentrations associated with pores and Lack of Fusion (LOF) defects and that the elimination of these defects would significantly increase the fatigue life [16]. These results have also been confirmed for Ti-6Al-4V samples where porosity of 5 vol.% of the defects is shown to be a limiting factor for mechanical properties acceptance produced with a high energy density. However, it has been found that defect occurrence at a rate as low as 1 vol.% has a considerable effect on mechanical properties. For LOF defects caused by lower energy density, even 1 vol.% of defects have been shown to strongly affect both tensile and fatigue properties [17], most likely due to stress concentrators (e.g., small radii of curvatures) in such defects. It was also found that defects closer to the surface affected fatigue life more, when compared to the defects that were deeper or far from the surfaces due to higher stress concentrations for the near-surface defects [16].

2.5.1 FACTORS CAUSING DEFECTS

Thermal stresses due to the AM process are the main cause of defects like primarily cracking and distortion [3], adding to factors stated in Table2.2 other parameters like laser power, scanning speed, hatching distance, layer thickness, and spot size also have significant effect in modelling the RS [18] literature also suggests on use of shorter scan lines [8], reduction of scan vector [9] and island scanning (which can result in a 40 % reduction in defects in AM). The mechanical properties of the final part are affected by and related to the specific manufacturing method used. Studies have investigated the influence of manufacturing methods and process parameters on finished part mechanical properties [19]. In addition to microstructural inhomogeneity's and mechanical property variation, the as-deposited density of AM components depends on powder characteristics, process parameters, layer thickness and scan line spacing. Laser power in the top range of the operational window results in higher density. Increasing the thickness of layers likely decreases the final part density unless the energy density is adjusted to account for the increase in melt pool depth required. However, several parameters limit the minimum layer thickness that can be employed, such as the maximum particle size. The powder spreading mechanism can disrupt previous layers when the layer thickness is close to or smaller than the maximum particle sizes. By decreasing scan speed and hatch distances (i.e., increasing energy density) the volumetric mass density of the resulting material increases, and, not surprisingly, has an influence on the mechanical properties. For example, the effect of layer thickness and scanning speed on tensile strength of 304L stainless steel samples was studied by [19]. Three different layer thicknesses (30, 50 and 70 μm) at two scanning speeds of 70 and 90 (mm/s) were considered. The samples with

higher layer thickness were more brittle in nature due to the occurrence of higher porosity [19].

In addition to high stresses related defects, other type of defect that can be found is un-melted particles formed due to the relation between speed of laser verses power of laser [7]. The relationship between speed and power that is needed to avoid defects varies depending on several factors: edge effects, scan strategy, part geometry and thickness of powder beneath the scan area. All these factors amount to changes in the initial conditions or boundary conditions for heat transfer. After a heat source passes near an edge, it may return to the edge before the heat from the previous pass has time to dissipate. The scan strategy can have a similar impact on heat flow, depending on how the strategy allows for cool down between each melting pass. Part geometry effects include those associated with a variation in the size of the part. A small part will reach a higher peak temperature during melting than a larger part, given constant power and speed. This can lead to more defects in smaller parts or features. For PBF, the state of the material underneath the melt area (powder vs. solid) can drastically affect heat transfer. A powder (non-sintered or sintered) has relatively poor thermal conductivity and can be considered thermally insulating compared to the solid part of the substrate. As heat is applied, it flows more slowly through the powder, which can lead to overheating of the melt surface located above the powder. The influence of all these phenomena means that applied power and speed alone may not be a simple factor to adjust.

As discusses earlier, the existence of defects can change final part material properties and quality. In-line monitoring and early detection of these defects will enable subsequent process control to modify the AM process, achieve higher deposition quality, and reduce

or eliminate avoidable costs. So, the focus of this paper is drawn on studying the various scanning patters and suggesting the optimized pattern from the results generated by digitally simulating the progressive element activation process in the ABAQUS software, further scope can be to physical test the results with actual physical model buildup and experimentation applying the scanning strategies. This work benefits from saving experimentation and guide the process development.

2.6 MITIGATING RESIDUAL STRESS AND DISTORTION

So, in brief two approaches to optimize residual stress is to closely control the process parameters defined in Table 2.2 and the second approach is the pre/post process methods like preheating substrate, heat treatment of the finished component [7]. Post heat treatment process is widely used to homogenize the microstructure and tailoring mechanical properties of as-build AM components and to increase the ductility at the expense of lowering tensile strength [20]. A post annealing of as-build AM part would reduce 70% of residual stress [10]. The maximum principal stress decreases as the powder bed preheating temperatures increases. Preheating temperature higher than 570 ℃ would result in zero residual [7] stress or even compressive residual stress which would be beneficial for fatigue performance.

2.6.1 SCANNING STRATEGY: (PROCESS PARAMETER)

Scanning strategy means any specific scan pattern or exposure method that is used to influence a dependent variable during the LPBF process. This includes, but is not limited to, different vector, segment, or layer scanning methods. The scanning strategy play a vital role in deciding the residual stresses as it is the major factor in accumulation of energy or heat distribution, it also has influence on surface quality and density of the

prints, if not designed properly it would lead to distortion, delamination, and balling defects [21], [22]. To deeply understand the effect of scanning strategy on SLM parts number of parameters associated with scanning strategy are to be keenly studied. Varying the size of the scan vector length, the orientation of the scan vectors, the order of scanning and the rotation of each subsequent layer can result in a significant combinations of scanning strategies [18] , [23].

In [18] the residual stress and distortion caused by 5 different scanning strategies are compared to pick the ideal strategy. The four strategies considered are a) 45° Alternating Scanning Pattern b) 90° Alternating c) Schematic of Chessboard Scanning d) Chessboard Scanning with Adjacent Chessboard block Scanned in 45° rotated direction. e) Chessboard Scanning with Adjacent Chessboard block Scanned in 90° rotated direction. These studies have concluded that samples built with 90° Alternating strategy proved to be the best for achieving minimum residual stress and resulted in 107 MPa as shown in Figure2.5. Chessboard scanning strategy showed a trend of increasing Residual Stress with increasing Chessboard blocks size Figure 2.6

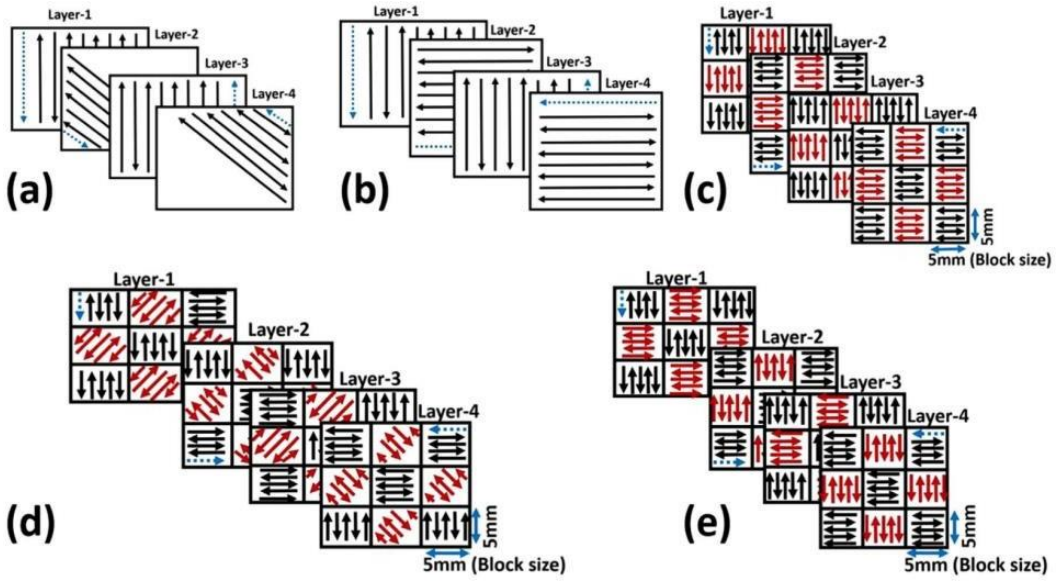

Figure 2. 5: Alternating scan pattern:
a) 45° Alternating (b) 90° Alternating (c) Schematic of Chessboard Scanning (d) Chessboard Scanning with Adjacent Chessboard block Scanned in 45° rotated direction. (e) Chessboard Scanning with Adjacent Chessboard block Scanned in 90° rotated direction [18]

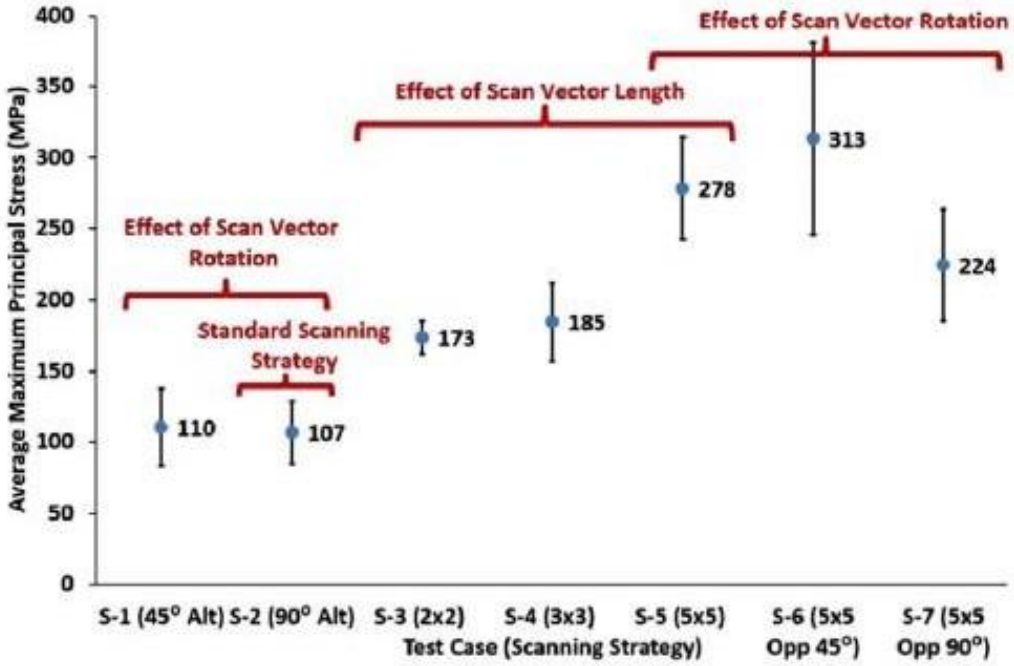

Figure 2.6: Effect of scanning strategy on residual stress

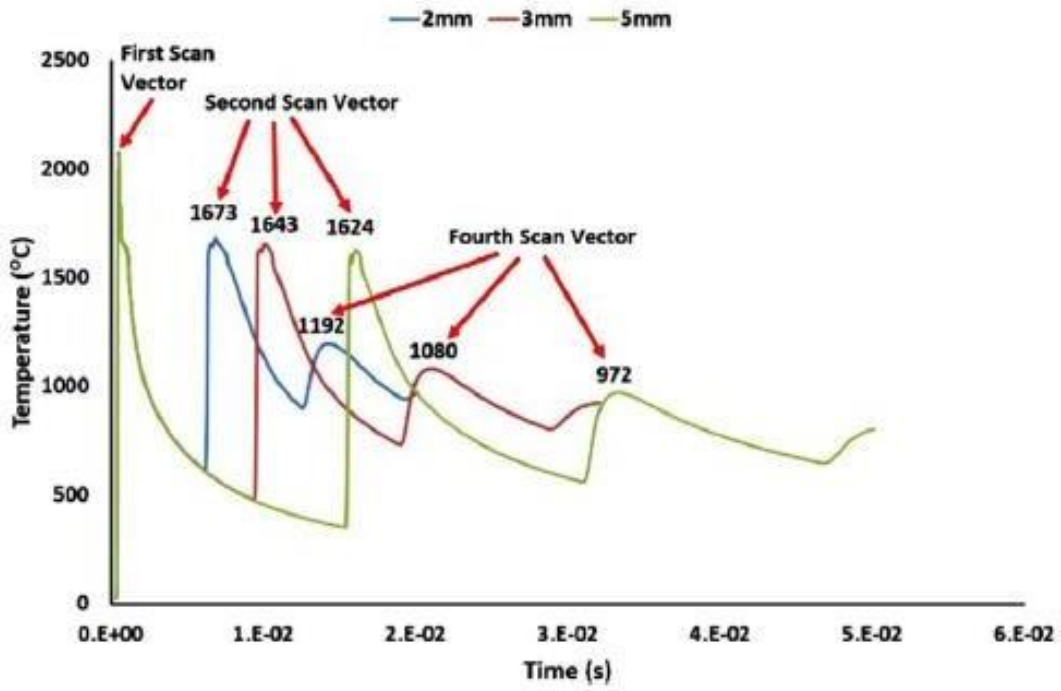

Figure 2.7: Effect of Scan vector
Figure 2.7: a) on Temperature

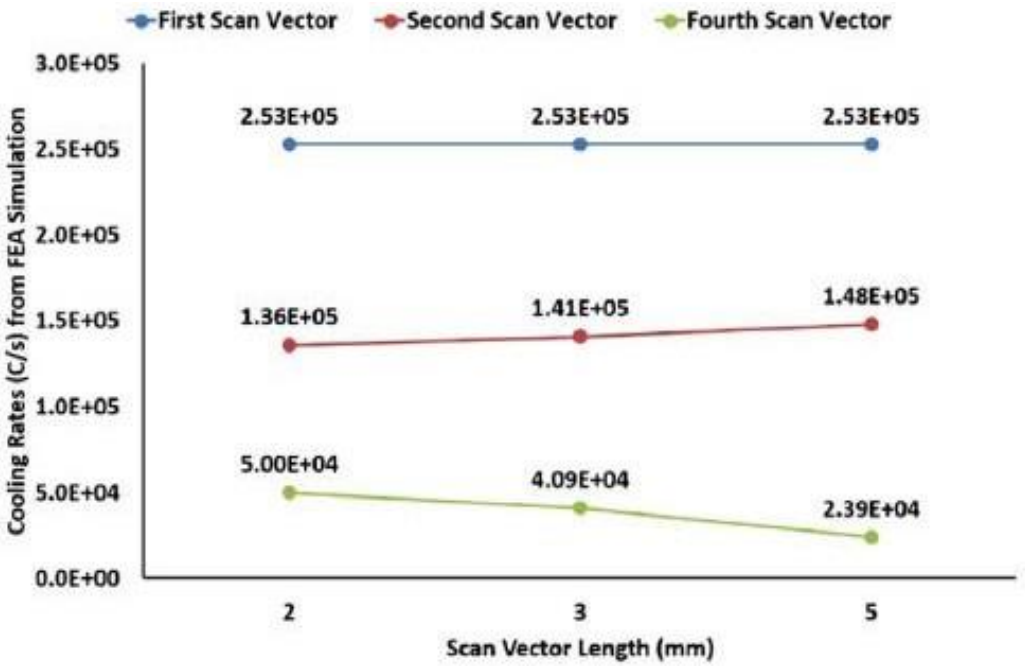

Figure 2.7:b) on cooling rate

The effect of scanning strategy on residual stress is complex and published literature shows varying effect of scan vector length and rotation on residual stress. The cooling

rates estimated from FEA simulation shown in Figure 2.7 also confirm the complexity of the relationship between scanning strategy and material behavior.

To understand the effect of scan vector length on the temperature of the powder bed FEA simulation with varying scan vector length was run to simulate six scan vectors. The temperature history of a point in the center of the surface of the first melt-pool was extracted from the FEA simulation. Figure 2.7(a) shows the temperature variation of a single point on the top center of the first melt-pool. It can be seen from Figure 2.7(a) that residual heat in already scanned region decreases with increasing scan vector length.

When the laser comes back to scan a region adjacent with the already sintered material it reheats the previously solidified material (re-scanning varying exposure). As the laser moves further from the sintered region of interest the effect of the laser on the temperature decreases. To better understand the effect of scan vector length on SLM parts cooling rates were calculated for the same spot based on the reheating effect from next scan vectors. Fig. 2.7(b) shows the effect of scan vector length on the cooling rate of the top center of the first melt-pool. It can be seen from Fig. 2.7(b) that the initial cooling rate of the melt-pool is independent of the scan vector length. When the laser comes back adjacent to the point of interest in the second scan vector it reheats the already sintered material as shown by the temperature history shown in Fig. 2.7(b). Increasing the scan vector length increases the cooling rate of the reheated sintered material. The laser comes back adjacent to the point of interest in the fourth scan vector and reheats the point of interest as can be seen in Fig. 2.7(b). It can also be seen that the cooling curve becomes less steep for the reheated sintered material with increasing scan vector length. Fig. 2.7(b) also shows that the sintered material reheated because of fourth scan vector adjacent to it cools slowly

with increasing scan vector length showing a complicated cooling behavior with varying scan vector length.

2.7 PREDICTION OF RESIDUAL STRESS

A right prediction saves lot of time and of resources, it gives a chance to optimize design before it is set for printing, it offers a chance to set the right parameters and scanning strategies based on the results from predictions of residual stress. Inherent Strain Prediction Method [24] is predominantly used in literature:

2.7.1 INHERENT STRAIN PREDICTION METHOD:

Main assumption of this methodology is that the main driving force for distortion is the linear thermal contraction of the melted metal on cooling. In welding applications, it is assumed that the material that is melted (weld bead) undergoes an equivalent thermal strain whose magnitude can be calculated by multiplying the material's thermal expansion coefficient and the temperature gap between surrounding material and melt pool. The inherent shrinkage methodology considers that this equivalent thermal strain must be accommodated by the part leading to a redistribution of stresses and strains. The mathematical equation of this approach is included in Figure 2.8

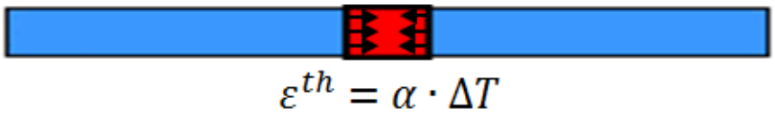

$$\varepsilon^{th} = \alpha \cdot \Delta T$$

Figure 2.8: Inherent strain

where ε_{th} is the equivalent thermal strain, α is the thermal expansion coefficient and **ΔT**is the temperature gradient, such method then is adopted in the LPBF widely.

2.7.1.1 RESIDUAL STRESSES: MECHANICS BACKGROUND

The fundamental governing equation for elasticity (i.e., reversible deformation) is Hooke's Law.

$$\boldsymbol{\sigma_{ij} = C_{ij\,kl}\,\varepsilon_{kl}} \quad (\mathbf{2.5})$$

where σ is the applied stress, C is the material's stiffness matrix, ε is strain, and i, j, and k denote 1, 2, and 3, independently. In the 3D Cartesian coordinate system, 1 corresponds to the x-axis, 2 is the y-axis, and 3 is the z-axis. In addition to mechanical loads, thermal loads can be related to strains in a body [24]. In this case, a change in temperature can cause a material to expand or contract, governed by the following equation:

$$\boldsymbol{\varepsilon_{th} = \alpha \Delta T} \quad (\mathbf{2.6})$$

where α is the material coefficient of thermal expansion, ΔT is the change in temperature, and ε_{th} is the thermal strain. The principle of strain superposition dictates that the mechanical strains (ε_{σ}) and thermal strains (ε_{th}) are summed to a total strain value.

$$\boldsymbol{\varepsilon = \varepsilon_{\sigma} + \varepsilon_{th}} \quad (\mathbf{2.7})$$

The total strain, given in the above equation, can used to obtain the stress in a part through the constitutive equation:

$$\boldsymbol{\sigma\, ij = \frac{E}{(1+\nu)(1-2\nu)}\left[\nu\delta_{ij}\,\varepsilon_{kk} + (1-2\nu)\,\varepsilon_{jj} - (1+\nu)\,\alpha\Delta T\delta_{ij}\right]} \quad \mathbf{(2.8)}$$

where E is the modulus of elasticity, is ν Poisson's ratio, and $\delta_{ij}$is the Kronecker delta, taking values of 0 for i , j and 1 for i = j.

After determining and mapping equivalent thermal strains in welded structures, a pure mechanical elastoplastic analysis is performed leading to the final distortion. Due to the layer-by-layer nature of PBF processes, the following assumption has been done in this work for the transference of inherent shrinkage methodology to AM: elements

included in one layer will undergo a shrinkage related to their thermal expansion when the metal is heated up to its melting temperature. Therefore, a full layer activation strategy [24] has been adopted which can greatly reduce FE-model complexity and computational costs in comparison with discrete shrinking elements. This methodology requires the FE-model with a sequential activation of layers or birth and death or model change technique [24]. In welding process modeling, the concept of applied plastic inherent strain has originally been proposed by [25]. It has then been largely used to reduce the computational time of the mechanical analysis in welding distortion prediction [26]. The principal steps can be summarized as follows:

1) High-resolution model of the transient thermo-mechanical analysis—this is usually performed on a smaller specimen of the workpiece.
2) Calculation of the plastic strain tensor components and the equivalent plastic strain once the whole domain has cooled down to the ambient temperature.
3) Transfer of the plastic strains obtained on the high-resolution model to the complete workpiece.
4) Elastic computation with the macro model to estimate the final distortions.

The main advantage of this method is the drastic reduction of computational time required for the mechanical analysis. Only a linear elastic solution is required for each time step. This method is not compatible with the local/global approach (see the "Thermal boundary conditions" section) since a very fine and accurate model is needed to determine the plastic strains. A thermal load applied on a coarse mesh would not be sufficient for this approach. Consequently, large modeling efforts must be accounted for during the initial transient thermo-mechanical analysis and for developing an efficient

field transfer tool. Moreover, it is compulsory to wait for the complete cooling of the domain before extracting the plastic strains; otherwise, the results will be inaccurate. This method was applied for the modeling of a cantilever build process and could analyze the effects of the laser scan strategy on the final distortions of the workpiece. Numerical results are in good agreements with the experiment. They also discuss a new accelerated mechanical simulation based on the assumption that thermal strains only affect the topmost layer allowing a reduction of distortion prediction computational effort to a few hours.

In this study, a coupled thermal-stress model that directly calculates thermal strain due to the thermal gradient was developed. This method, as an alternative to the inherent strain method, eliminates the inaccuracy of temperature-dependent non-linear strain values, but may yield high computational cost. The methodology of the development method is discussed in Chapter 3.

CHAPTER 3 MODELING METHODOLOGY

In this chapter, two modeling methods for the prediction of residual stress are detailed: one is based on layer-by-layer activation, which developed in this thesis; and another method is based on progressive element activation, which is provided in ABAQUS. In this way, we can predict, optimize and design efficient processes and strategies to effectively foreseen the residual stress and compensate the distortion.

Table 3.1: Types of FEA simulation approaches

Methodology; FEA- RS Simulation	Layer -Layer Activation (Model Change)
	Progressive Elemental Activation

3.1. MODEL CHANGE METHOD (LAYER- WISE ACTIVATION):

Layer-Layer Activation [27] is carried out using a commercial finite element package ABAQUS 2020 was used to setup and solve the thermal-displacement coupled analysis. A model change method allows to deactivate and reactivate elements to simulate removal of part of the model, either temporarily or for rest of the analysis. The model must be meshed and divided into multiple print layers based on the thickness of the part and the grain size. The layers are then grouped together based on the order of De-activation or activation procedure. Then the assigned layers are activated/De-activated in specific Steps as defined by the process. The activation and De-activation are controlled by the Model Interaction definition.

3.1.1 THERMAL-MECHANICAL COUPLED ANALYSIS

The macroscale part model is a thermal-mechanical coupled analysis which has two analysis steps. Step one is to conduct the thermal analysis from which the temperature field for the whole process was captured. Step two is to perform the mechanical analysis which is used to calculate the stress distribution of the model. The temperature calculated from step one was applied as the thermal load for step two. The mechanical response including part distortion of the model to the thermal load was obtained in this step. For the mechanical analysis in step two, the governing equation for Gaussian heat [28] source is given by Eq. (3.1), the equivalent body heat flux is applied over the entire layer:

$$\mathbf{q} = \frac{\mathbf{Ap}}{\mathbf{d_s d_m H}} \qquad \textbf{(3.1)}$$

where ds is the laser spot diameter, dm is the melt pool depth, and H is the hatch spacing stress. Stress can be calculated from the data of Eq. 3.1 at various nodes.

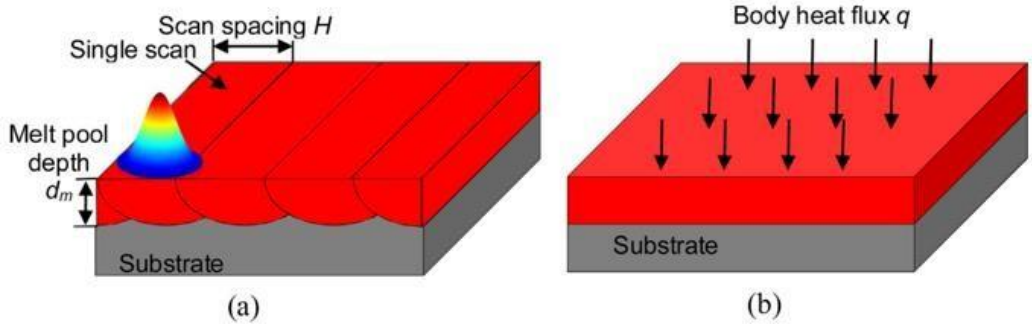

Figure 3.1: Body heat flux [28]

3.1.2 PARAMETERS CONSIDERED FOR LAYER - LAYER ANALYSIS

To maintain consistency and accuracy, the following parameters are required to be defined:

1) Laser Power, Speed,
2) Layer Thickness, Hatching Distance, Angle of Rotation,
3) Material Properties of Powder
4) Mesh Size, Element Type
5) Boundary Conditions

In this analysis laser power of 190 W, with Scanning speed of 1 m/s is used. The materials used is of IN625, a Nickel-based superalloy with density 8840 kg/m^3 and layer thickness of 30µm, the substrate is of SS-304. Table 3.2 discusses properties in detail, Figures 3.2 depict temperature dependent properties of IN625. A tetrahedron element C3D4T temperature-coupled displacement element is used for the analysis.

Table 3.2: Process parameters and simulation conditions

Part material	IN 625
Build plate material	SS 304
Laser Scan speed (mm/S)	500
Laser Power (W)	125
Laser Spot diameter (mm)	0.08
Laser absorption	0.35
Ambient temperature (*C)	20

Hatch Spacing (mm)	0.10
Layer Thickness (mm)	0.03
Powder spread time (s)	5
Re-coater time between layers (s) (cooling time)	15
Build plate temperature (*C)	100
Heat transfer Coefficient (metal/powder) W/m^{2}K	10
Heat transfer coefficient (build plate/ environment), W/m2/K	15

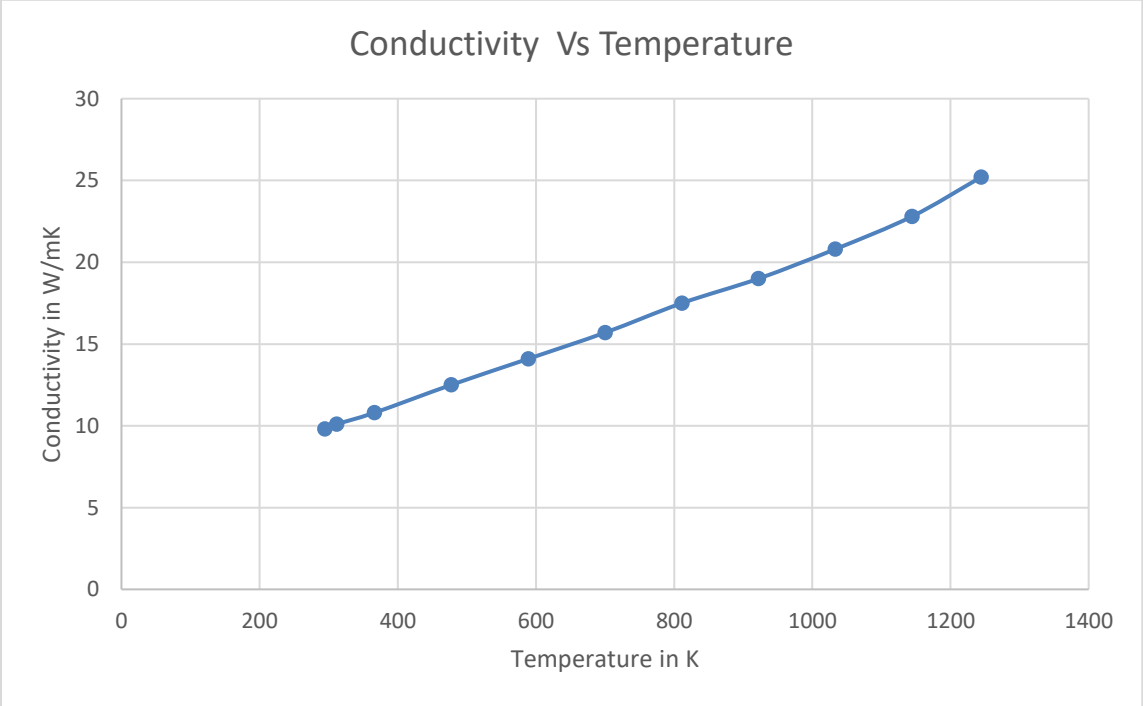

Figure 3.2: Material properties of IN-625 [30]
Figure 3.2:a) Thermal Conductivity

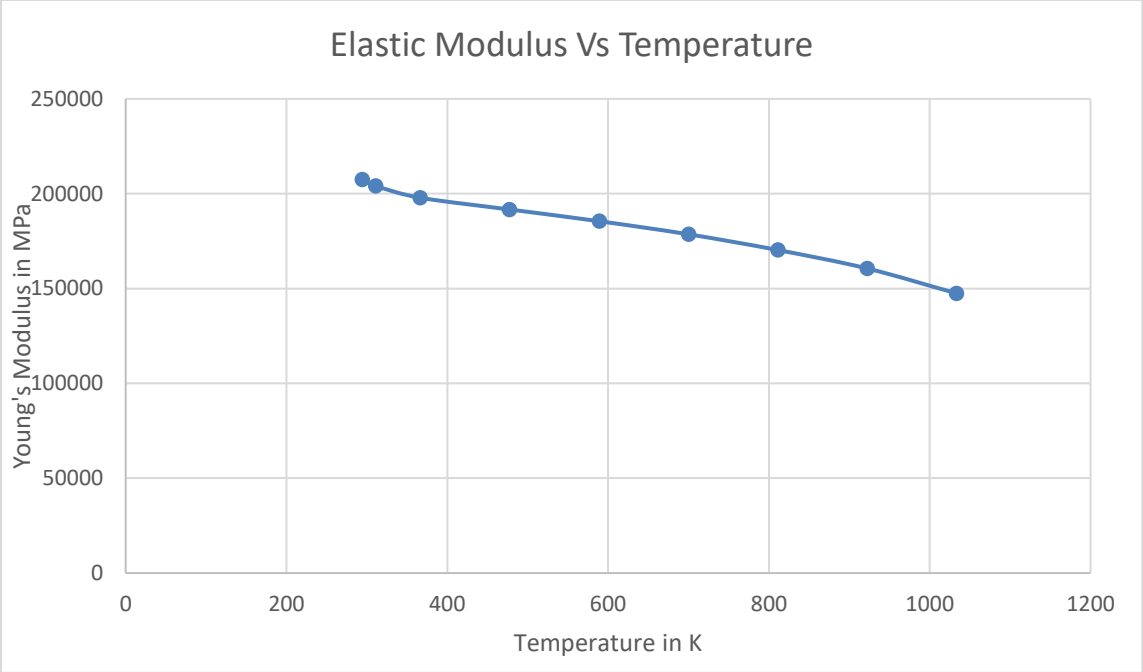

Figure 3.2:b) Youngs Modulus

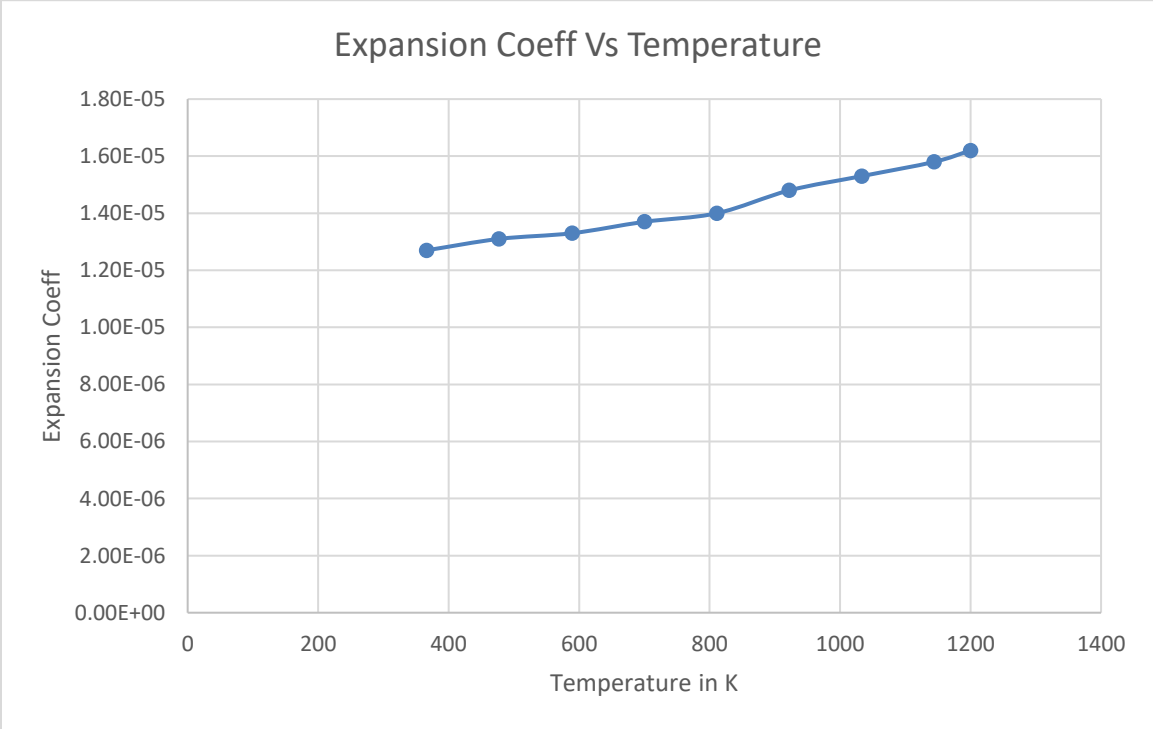

Figure 3.2:c) Expansion Coefficient

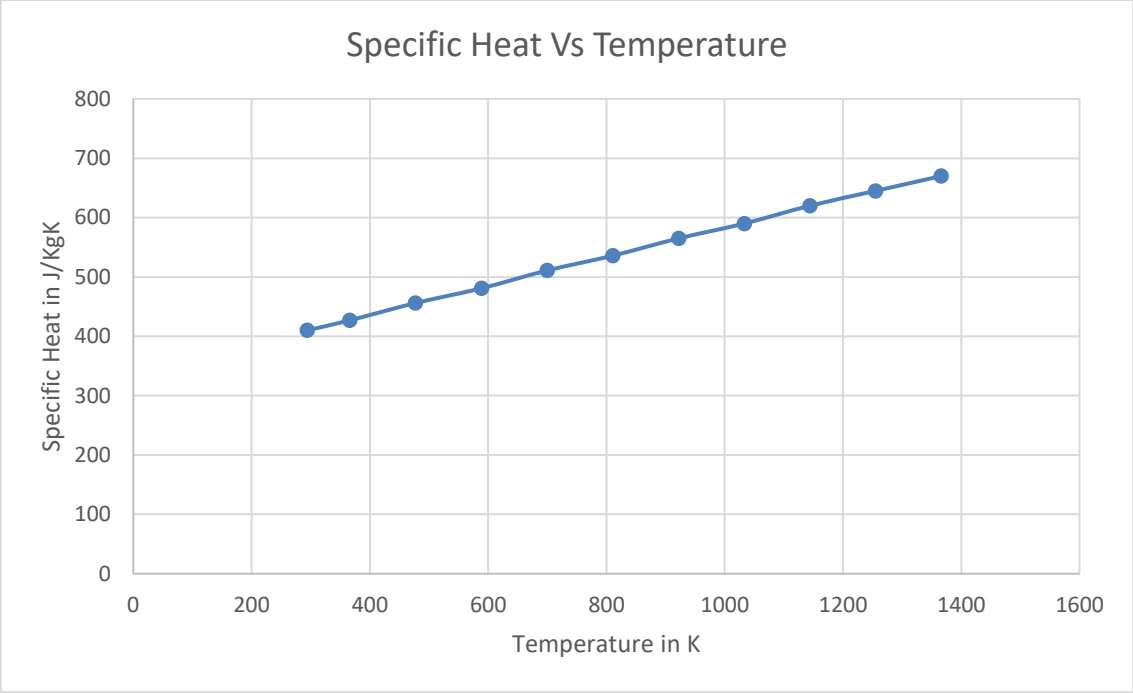

Figure 3.2: d) Specific Heat

3.1.3 LAYER -LAYER PROCESS WORKFLOW

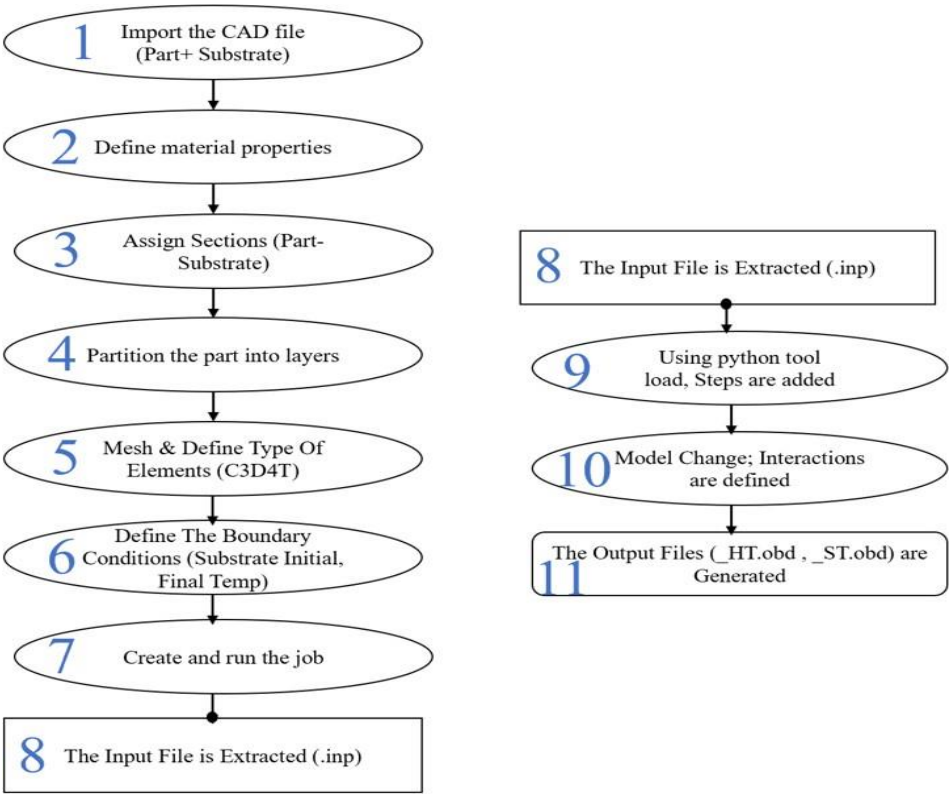

Figure 3.3: Workflow model change

The process begins from 1 as in Figure 3.3. importing a designed CAD model, 2. material properties are then defined respectively for Part and Substrate. 3.Then two respective sections are created and assigned to the part and the substrate to link the material properties with the part and substrate. Now by dividing the total height of the part and the powder thickness we get total number of physical actual layer involved, to optimize the computational efficiency we consider 10actaul layer as to 1 simulation layer, based on this we divide the and 4. create partitions of the part using reference planes. Once partitions are created 5. we mesh the part and substrate using Tetrahedron mesh and C3D4T thermo-coupled element type.

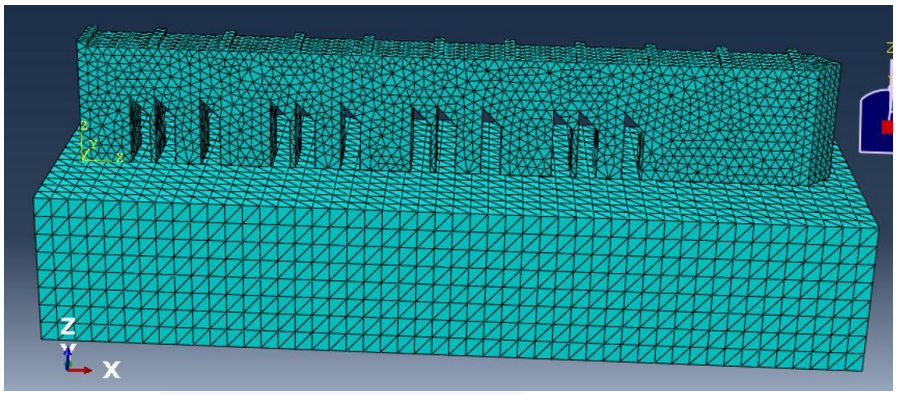

Figure 3.4: Part and substrate meshed

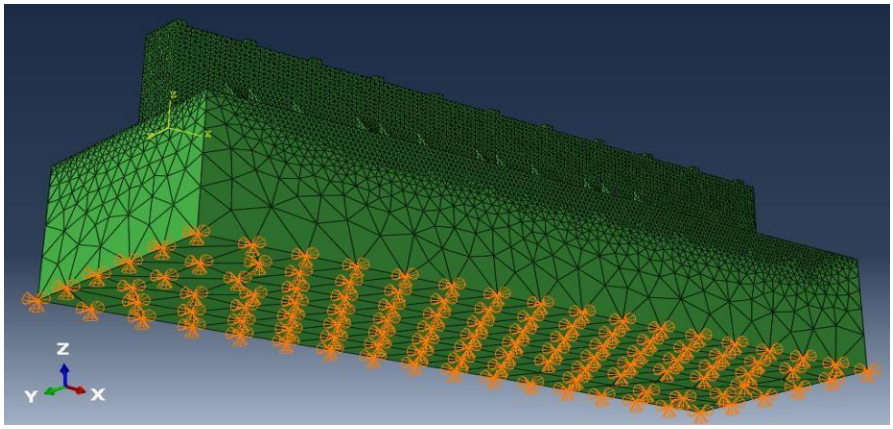

Figure 3.5: Substrate boundary condition

In step 6. We create en-caster (U1=U2=U3=0) boundary conditions as shown in Figure 3.5, in 7. input file is written for the model and file is exported in '.inp' format. The model change interaction, which is explained in Chapter2, section 2.7.1 [24] is primary for simulation of AM build process in 8. Using a Python tool sequential steps and loads are defined and attached to the model, the step time is calculated by the tool based on the speed of laser scans and the recoating time, during the odd steps (Step1, Step3...Step51) laser prints (power imparted to the system) and during even steps (Step2, Step4...Step52) are for recoating time and cooling time before laser scans next. Python tools creates the required sequential steps as above. Similarly loads are also created based on Gaussian heat [28] source is given by Eq. (3.1). The model change process is operated by setting the interactions sequence, as in LPBF AM process part is constructed from powder by layer-by-layer melting and solidification, so the model change interactions activate respective layer only when they are printed during the odd steps. Finally, in flowline at 11. python tool gives two output files HT.obd and ST.obd containing the NT11(Temperature profile) and S, U (Max/Min Stress, Displacement) which can be further loaded into ABAQUS for Post-processing various simulation results.

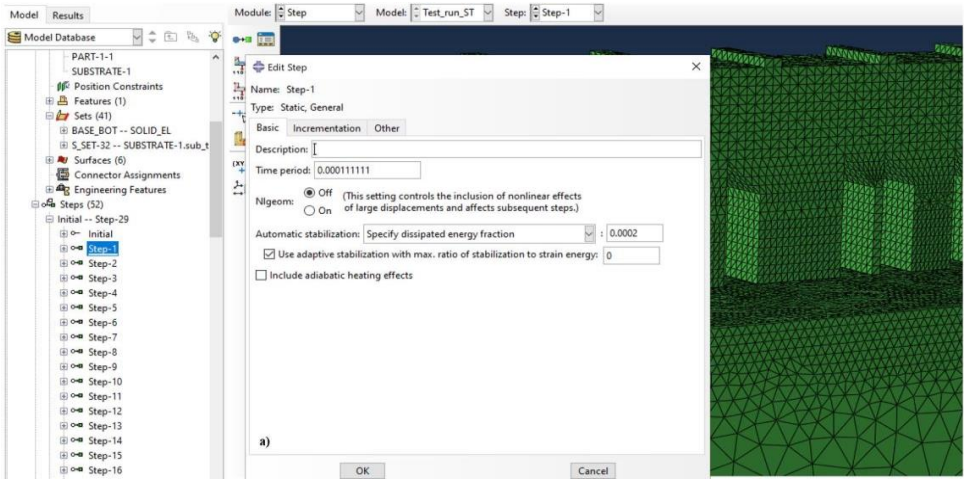

Figure 3.6: Steps: step-1(odd Steps) time periods

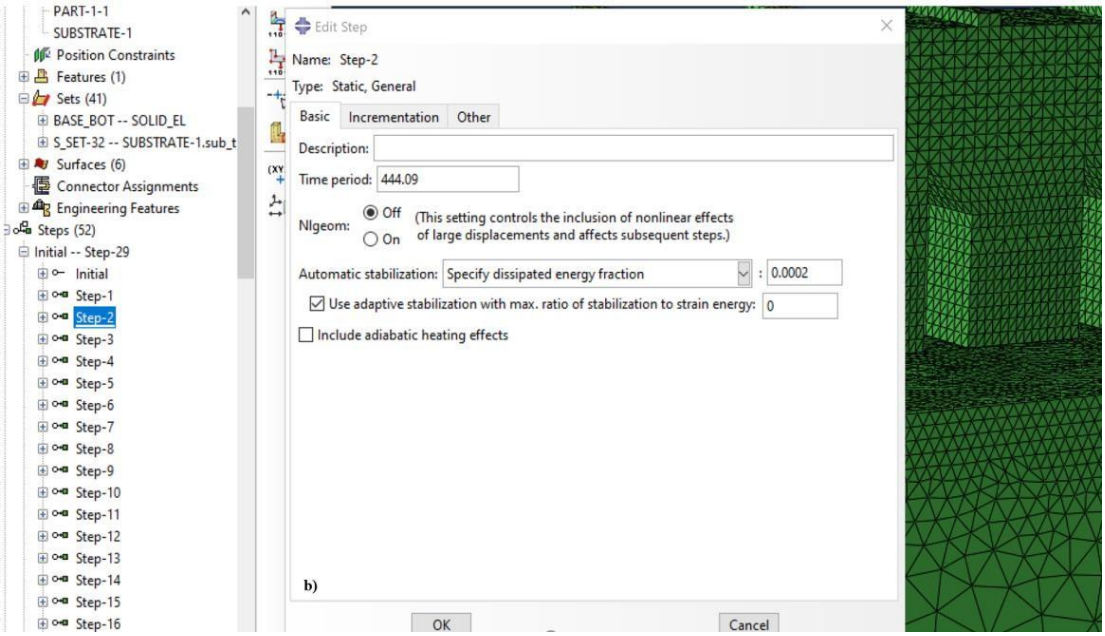

Figure 3.6: Steps step-2(even steps) time periods

3.1.4 LAYER ACTIVATION INTERACTION PROCESSES

At the beginning all elements representing the powder layer are deactivated [29], i.e. they cannot physically interact with other elements. When the heat source starts its movement, elements at the current heat source position are activated. As far as integration points in powder material elements reach melting temperature, the properties are changed to those of the bulk material (like in the heat source model). The mechanical properties of the powder are as follows: the yield stress is zero (representing an inelastic behavior), the thermal expansion is zero (powder is loose), and the Young's modulus is something above zero (it cannot be exactly zero due to back-stress calculations for plasticity).

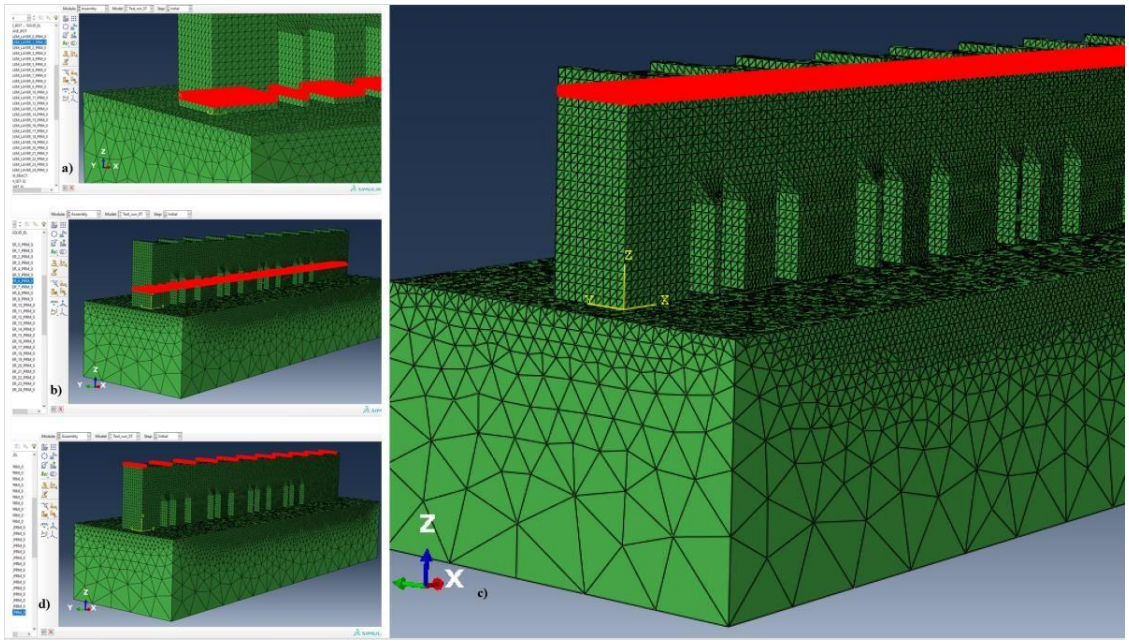

Figure: 3.7: Layer-wise partitioning
a) elemental set of 2nd layer b) 6th layer c) 23rd layer d) 24th layer

Furthermore, standard convection and radiation boundary conditions are also considered. A fixed displacement boundary condition is applied on the bottom of the substrate plate. In theory an entire powder layer must be activated at once and partially consolidated by the heat source. Since the thermal strains lead to high deformation of the deactivated elements, this activation procedure is not feasible due to numerical problems. However, the heat conductivity of the surrounding powder is neglected in this model, but mechanical consolidation is considered. The missing thermal expansion of powder material until the melting temperature is reached results in higher strains which represent the difference between the processes of “pure” welding (as re-melting process) and deposition welding.

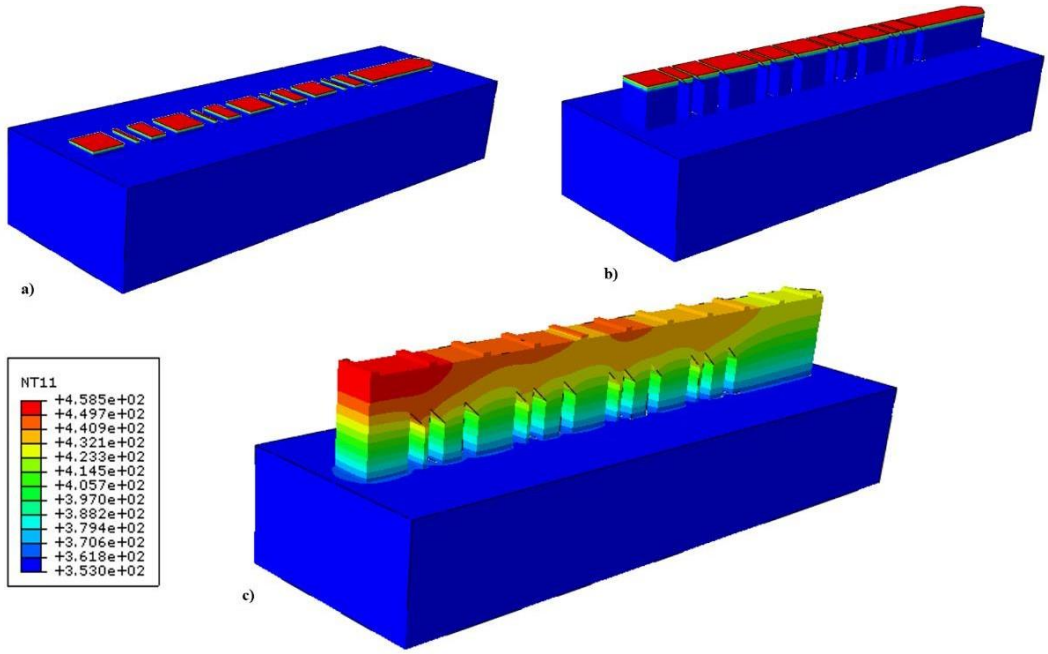

Figure 3.8: Layer wise activation
a) activation of 2nd layer, b) 6th layer, and c) 24th layer

Here commercial finite element package Abaqus 2020 was used to setup and solve the thermal-displacement coupled analysis. Four-node, coupled-temperature displacement, reduced-integration elements (C3D4T) was used. The process parameters and the boundary conditions in Table 3.2 and Figure 3.2 were applied to simulate the build process of the thin structure. The detailed temperature-dependent materials properties for as-build samples are discussed in Chapter 4. The predicted temperatures at various stages are shown in Figure 3.8 (c). The model started with the build plate with a predefined initial temperature at 100 °C. Each element layer was set to consist of 10 actual build layers. These were activated with zero-stress and zero-strain and with an initial temperature condition at predefined times corresponding to the actual build process. Figure 3.7 (a)-(c) show the activation of the layers. Due to the heat flux applied to the top layer body, high temperature is exhibited at the top layer and then heat is conducted away gradually. High stress levels were predicted at the interface region between the part and the build plate due

to the dissimilar joint between materials. The build-up and distribution of the stress reaches equilibrium in the main body of the part, while the stress gradients are profound near the side and top of the part due to the large thermal gradients in these regions. Once the part was completely activated, the part and build plate were naturally cooled down to room temperature, and the final residual stresses in the as-built geometry were predicted.

3.2. PROGRESSIVE ELEMENT ACTIVATION METHOD:

In this method the elements are activated in each increment of a step. Elements to be activated during an analysis are to be defined before they can be activated and then refer to them in each analysis step in which they can be activated. Event-Series created from the G-code operates the elemental activation and de-activation.

3.2.1 PROGRESSIVE ELEMENT ACTIVATION PROCESS

PEA process is split into Three steps: 1) Setting up the Thermal and Mechanical '.cae' model 2) Slicing part and generating Event-Series data for laser path and material deposition path 3) Linking step1 model with step2 data using AM modeler plug-in.

3.2.1.1 SETTING UP THE THERMAL AND MECHANICAL

Initially part is loaded into ABAQUS2020, and the process as defined in the Figure 3.4 step 1-3 are similarly carried out till assigning the material and properties to the part and substrate. In Progressive Elemental Activation (PEA) the elements used for mesh are DC3D4 for Thermal analysis and C3D4 for Stress analysis we need to create two separate models unlike Layer-Layer method where we use only Thermo-coupled displacement. For both the models (Thermal, Mechanical), steps (Heat Transfer, Static General) and substrate encaster(U1=U2=U3=0) boundary conditions are to be defined. Two job one for Thermal model and one for Stress model are created and submitted.

3.2.1.2 CREATING EVENT-SERIES

A part is initially designed using CAD software and then it is loaded into NETFAB for slicing and designing the scanning strategy. Various parameters like

1) Laser Power
2) Scan Strategy
3) Hatching Distance/ Angle
4) Orientation

Which influence the temperature profile during the printing are set here and '.lsr' file format is exported to create Event-Series. A Python scrip is used to generate two G-code files for Event- Series files of material addition path and laser scanning path. Thus these two files are used by AM-modeler Plug-in.

3.2.1.3 SETTING-UP AM-PLUGIN

These two files are fed to ABAQUS AM-Plugin as '.inp' files at step 1 in Figure 3.9. further at steps 2, 3 this data is linked to the laser and material deposition tables and the model is setup. The absorptivity and radiation coefficient are collected at step 4-6 and the AM-model is set.

Now, the Thermal and Mechanical models can be submitted and run to get the .odb files which gives the NT11 (Temperature Profiles) S,U (Stress and Displacement) are obtained from the results.

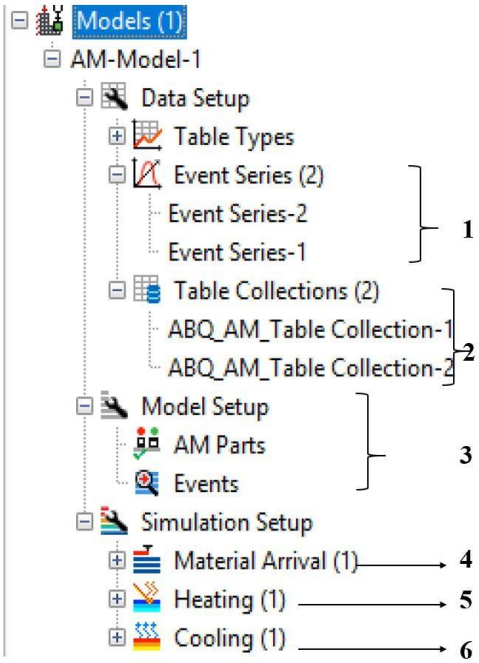

Figure 3.9: AM modelling plug-in

3.2.2 MATERIAL AND LASER ACTIVATION STRATEGY

In the Layer-wise activation strategy, the entire layer is activated at a particular step, but in PEA activation of elements is more controlled and precise. This is achieved by the generated Event-Series. In the G-code files Figure 3.10 T1- time step in s, x1,y1,z1 are the co-ordinates of the re-coater, 1,0 represents activation, deactivation, P stands for power of laser. So, the elemental activation depends on 1 and 0.

For full activation, the material volume fraction added must be equal to 0 or 1 (that is, the status of an element can change only from inactive to fully active). For partial activation, the material volume fraction added can be arbitrary; however, in practice the volume fraction in an element should not be too small to prevent numerical singularity

GcodeMaterial.inp

```
0,-1,-1,2e-05,1
1.0,1,1,2e-05,0
40.4498414083,-0.1,-0.1,4e-05,1
41.4498414083,0.1,0.1,4e-05,0
80.9851141291,-0.1,-0.1,6e-05,1
81.9851141291,0.1,0.1,6e-05,0
121.5694268028,-0.1,-0.1,8e-05,1
122.5694268028,0.1,0.1,8e-05,0
```

T1, x1, y1, z1, 1
T2 , x2 ,y2 ,z2 ,0

GcodeLaser.inp

```
1.0,0.0,0.000141,2e-05,200
1.0001994041,0.000141,0.0,2e-05,200
1.0005155844,0.0,0.000283,2e-05,200
1.0009158069,0.000283,0.0,2e-05,200
1.0014255764,0.0,0.000424,2e-05,200
1.002025203,0.000424,0.0,2e-05,200
1.0027324031,0.0,0.000566,2e-05,200
1.003532848,0.000566,0.0,2e-05,200
```

T1, x1 ,y1 ,z1 , P

problems. In stress-displacement analyses it is assumed that the material added to an

Figure 3.10: G-code material, laser

element is stress free. Therefore, for full activation the configuration at which an element is activated is the stress-free configuration from which the strains used to compute the material response are measured. For partial activation, the newly added material, and the material already present are at different states. To obtain the material response, Abaqus/Standard uses the rule of mixtures to compute homogenized state variables.

Elements for which the activation feature is turned on in a step can be activated by assigning a volume fraction of material to an element at the beginning of each increment. The element can be both fully and partially activated. Elemental activation is dependent on the event series files generated by the G-code depending on the laser scanning strategy. Elements can be activated in each increment of a step. Elements must first be defined then they can be activated during an analysis and then refer to them in each analysis step in which they can be activated. Elements for which the activation feature is turned on in a

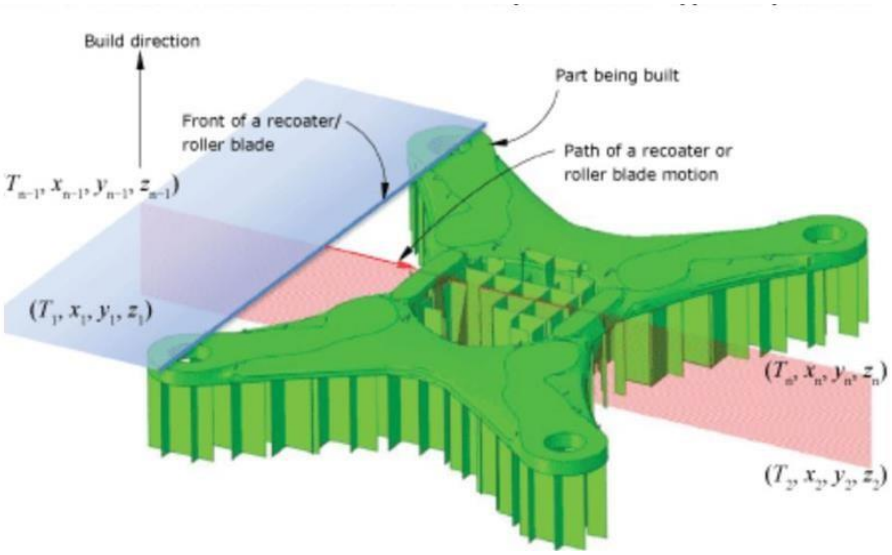

step can be activated by assigning a volume fraction of material in the

Figure 3.11: Elemental activation from event series data

element at the beginning of each increment. Elements cannot be partially activated; therefore, the material volume fraction added that you specify must be equal to zero or one, which means that the status of the element can change only from inactive to fully active.

CHAPTER 4 MODEL VALIDATION VIA BENCHMARK CASE

A cantilever structure of dimensions 75 mm, 5 mm, and 12.5 mm in length, width, and height, respectively is selected for this study. Supporting literature [30] studies and benchmark data can be found at NIST website[32]. In this Chapter 4 the analysis focuses to predict residual stress and distortion (displacement) in the part model.

A 2-D and 3-D depiction of the geometry can be seen in Figure 4.1 and Figure 4.2. Within the benchmark, the part was built with IN625 and substrate with SS-304 Stainless Steel. Temperature dependent material properties are used in the model, which are collected based on the data from literature[33]. The material properties used within the model has been described in section 3.1.2, Figure 3.2.

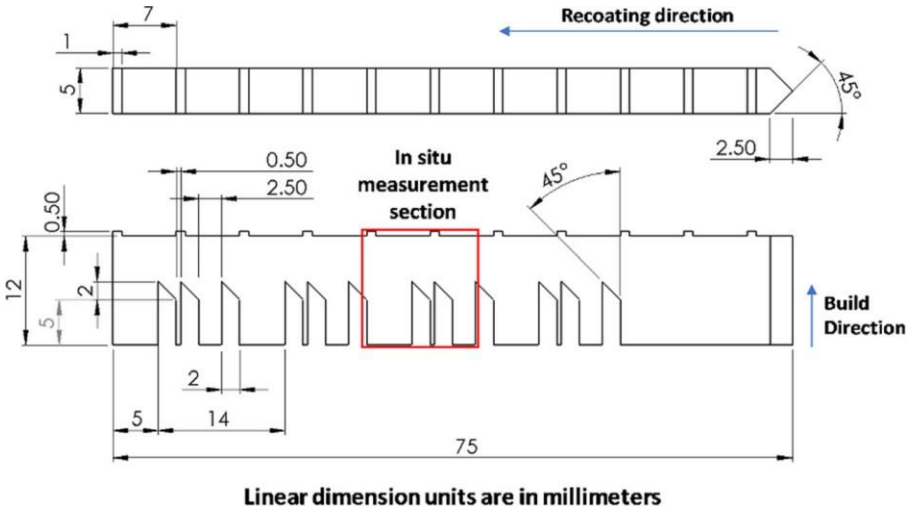

Figure 4.1: 2-D model of bridge profile

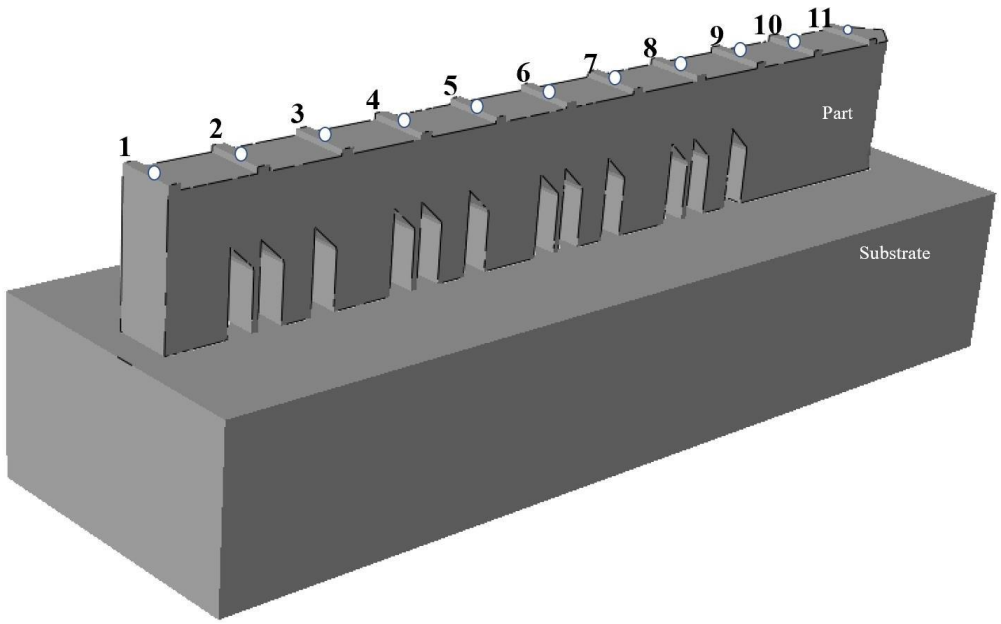

Figure 4.2: 3-D model of bridge profile with substrate

4.1 PART DEFLECTION: BENCHMARK NIST-AMB2018-01

For these benchmark comparisons, the part distortion is defined by the vertical deflections of all measured ridge edges (1-11) Figure 4.2. Thus,

$$\boldsymbol{\delta_i = Z_{i_{(after)}} - Z_{i_{(before)}}}, \quad (4.1)$$

where Zi is the vertical deflection of edge i.

As shown in the Figure 4.1 the width of the ridge is 5mm and length is 1mm, the center of these ridge profiles is considered for study, points are marked exactly at the center of the ridge profile at 2.5mm, 0.5mm along the width and length, respectively.

Thus, deflection is calculated at these 11 points represented in Figure 4.2 using Eq. 4.1.

before and after the EDM cut simulation to get values of Z_i before and after and compared with benchmark results. The deflections results are plotted on a graph as in Figure 4.3.

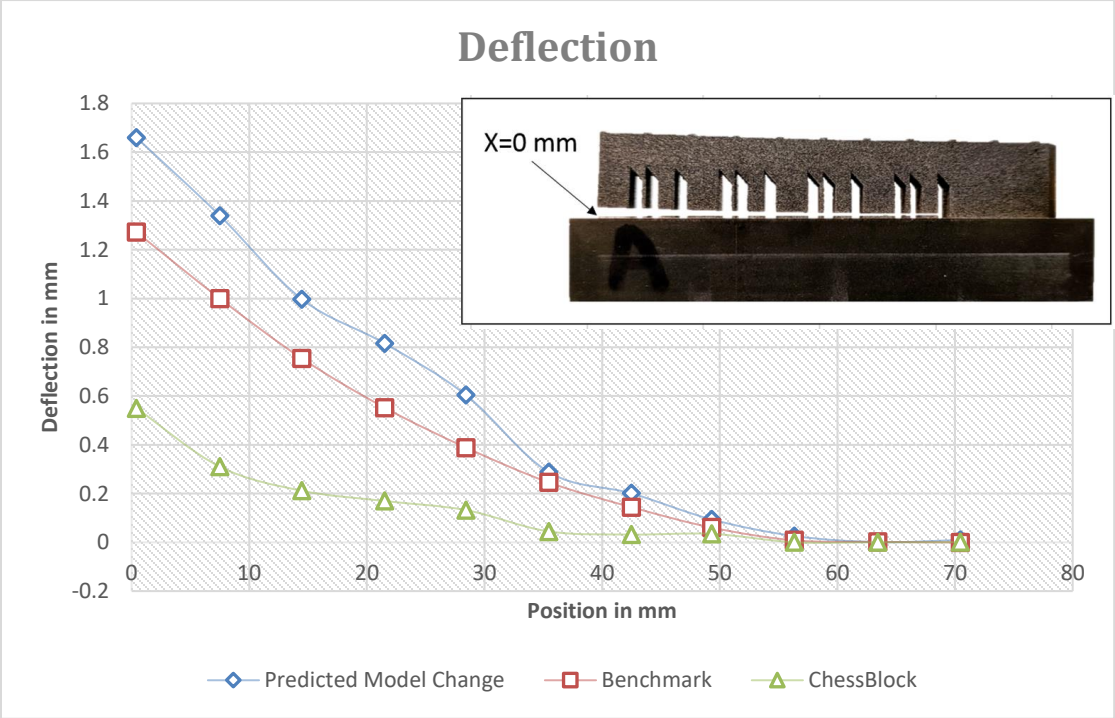

Figure 4.3 Deflection comparison benchmark results Vs model change prediction, PEA

Table 4.1: Error ratio benchmark Vs model change, PEA

X (mm)	LWMC	PEA
0.41	0.3	0.56
7.49	0.34	0.68
14.47	0.32	0.71
21.5	0.47	0.69
28.42	0.55	0.65
35.45	0.17	0.81
42.49	0.39	0.77
49.3	0.54	0.42
56.33	0.68	0.94
63.42	0.55	0.77
70.45	0	0

Figure 4.3 specifies the deflection results of Benchmark model as red curve, Model Change prediction as blue curve and PEA as green curve. The maximum deflection obtained in benchmark model is 1.27mm at point 1 where X=0, with following consequent deflections as 1mm, 0.75mm, 0.55mm, 0.38mm, 0.24mm, 0.14mm, 0.06mm, 0.008mm, 0.002mm, 0mm at points 2 -11 respectively. While maximum deflection for the Model change prediction being 1.66mm at point 1 where X=0mm, with consequent values being 1.34mm, 0.99mm, 0.81mm, 0.6mm, 0.28mm, 0.2mm, 0.09mm, 0.02mm, 0mm, 0mm at points 2-11 respectively. So, from the above graph both the benchmark model and the model change prediction method both follow similar trend of deflection with the maximum offset of 0.39mm at point 1. The deflection profile of model change method is shown in Figure 4.4.

Observing the values of PEA from the green curve a maximum deflection of 0.55mm is at starting point 1 where X=0, following 0.31mm, 0.21mm, 0.17mm, 0.13mm, 0.04mm, 0.032mm, 0.035, 0mm, 0mm, 0mm at points 2-11 respectively. Comparing these values with benchmark values we see similar trend in the graph, but the deflection is underpredicted by highest offset of 0.7mm. The deflection profile of model change method is shown in Figure 4.5 and the error ratio between benchmark model and Layer-wise model change (LWMC) method and PEA are tabulated as in Table 4.1.

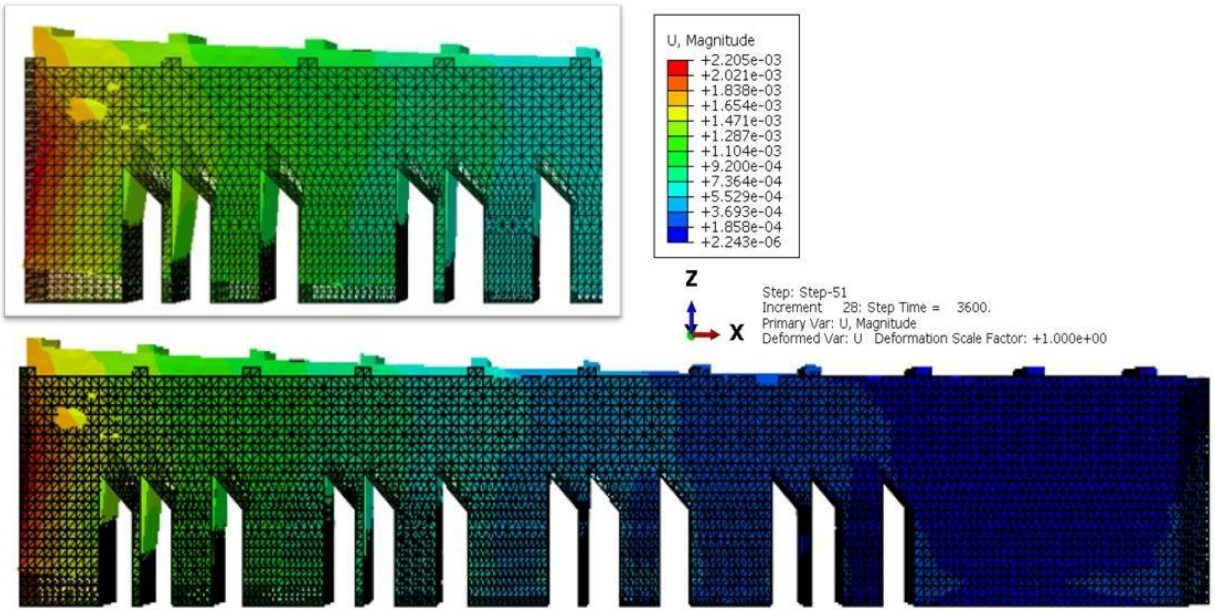

Figure 4.4 Deflection profile in model change method (detailed)

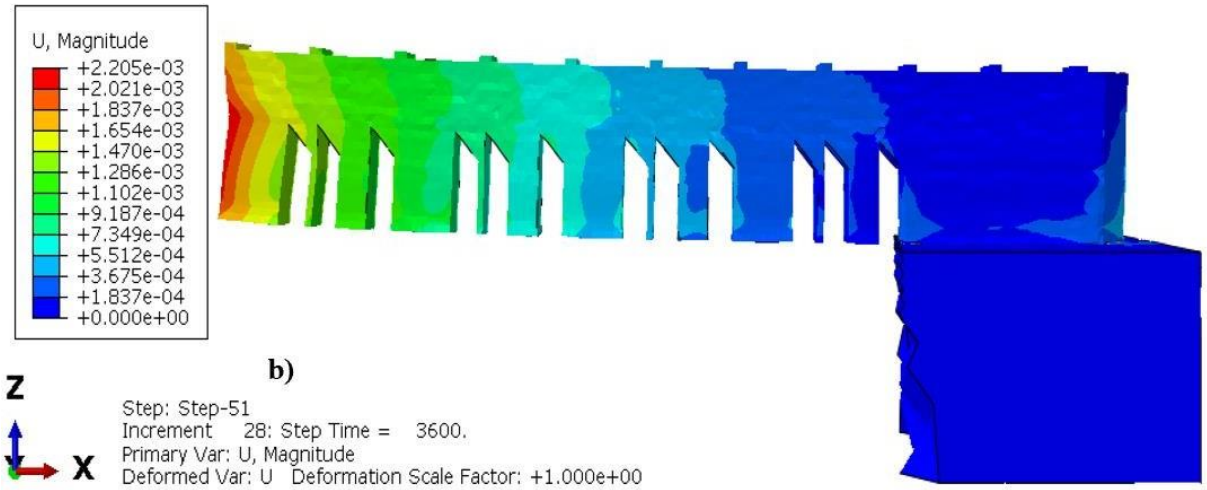

Figure 4.4 Deflection profile in model change method (overall)

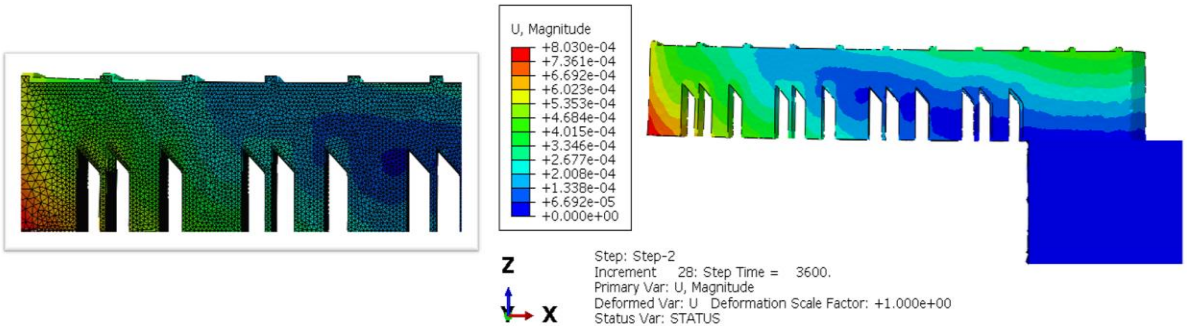

Figure 4.5: PEA method deflection

4.2 STRESS PREDICTIONS

Figure 4.6 represents the stress profile of the cantilever beam after that is cut off from the substrate. The gradients of red shaded regions represent the zone of high stress, from the Figures 4.6 a-b the maximum von Mises stress for model change predictions was 990Mpa and that of PEA was 784Mpa. Observing the overall trend, the high stress regions are observed at the surface's contacts between the 1st layer and the substrate, at the intersection of pillars with the beam, and at the topmost surface of the bridge model. Results are thus validating with the literature that entrapped thermal gradient causing residual stress [9], [10].

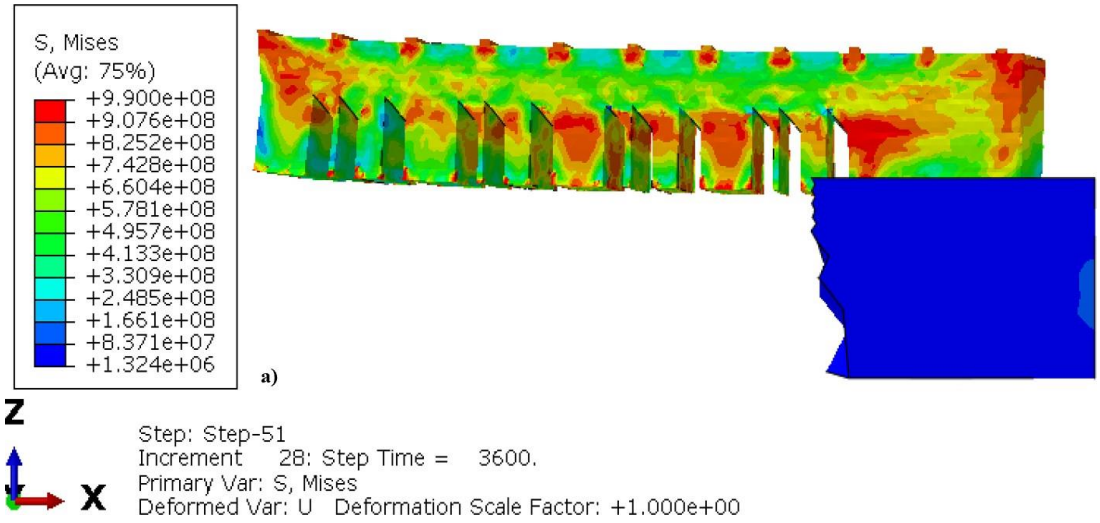

Figure 4.6: Stress profile - model change method

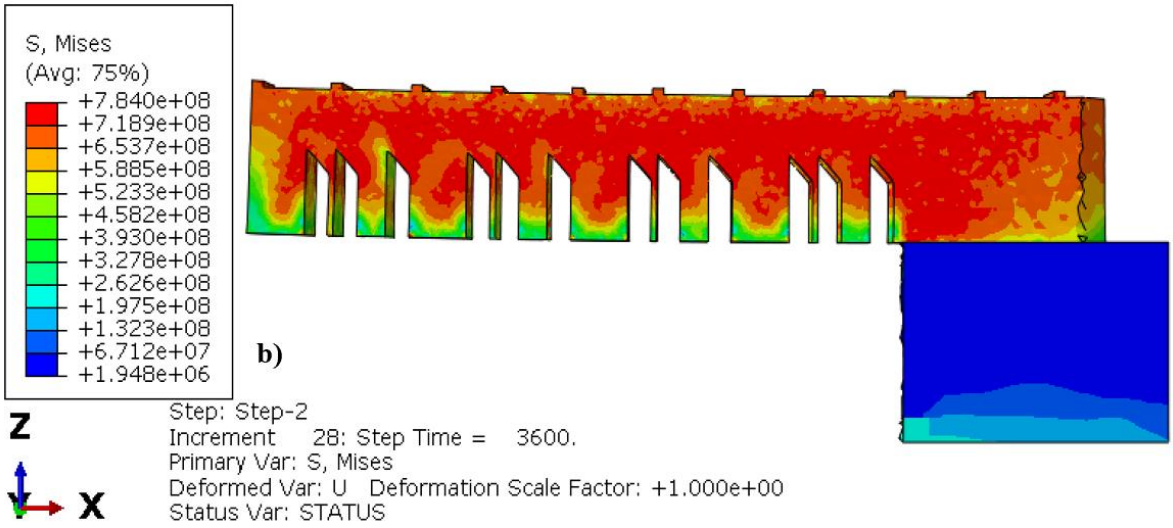

Figure 4.6: Stress profile - PEA method

Primarily the deflection or displacement results are converging with the benchmark results, the von Mises stress profiles are extracted to represent the stress distribution. The factors causing stress were briefly discussed in literature [14] were validated in this model, coming to deflections, a small offset of 0.4mm which is a reasonable variation considering approximation error in temperature dependent material properties, mesh size and refinement, laser scan pattern design. If this stress exceeds the local yield stress of material, warping or plastic deformation occurs.

However, there is a need for further investigation to check the reasons why there is an offset of 0.7mm or 55% under prediction between the benchmark and PEA results.

For printing of same cantilever design with same parameters by layer wise model activation method and PEA methods there was variation in prediction of deflection and stresses (Section 4.1,4.2), which should ideally not occur, but the accuracy of predictions and repeatability depends on accuracy in selection of: refinement of the mesh, size of the elements and temperature dependent specific material properties.

CHAPTER 5 APPLICATIONS

In this chapter we discuss about the application of layer-wise model change method to two other models to find out the deflection due to residual stress, stress distribution and temperature distribution profile. The models considered are: 1) Al10SiMg printed Channel Plate and 2) PLA printed dog-bone structure using fused filament fabrication.

5.1 CHANNEL PLATE ANALYSIS

A Channel Plate of 91.14mm ,40mm,2mm length, width, and height was considered as the base, upon which 19 thin bars of dimensions 59.75mm,1mm,1mm in length, width, and height, are respectively selected for this study. The Channel Plate is printed using LPBF manufacturing process. The Layer wise model change method as described in the methodology is used for analysis here. The material properties, boundary conditions considered are described here.

5.1.1 DEFINING MATERIAL PROPERTIES

The Channel Plate and Bars are built with Al10SiMg material, the temperature dependent material properties are defined below in Table 5.1 -5.2

Table 5.1 General Material Properties

Temp in K	Thermal Conductivity (W/mK)	Young's Modulus MPa	Poisson's Ratio	Expansion Coefficient	Specific heat (J/kgK)
293	113	7.76E+4	0.33	2.00E-05	739
373	155	7.28E+4	0.33	2E-5	754
473	159	-	-	2E-5	796
573	159	-	-	2E-5	837
673	155	-	-	2E-5	921
323		7.55E+4	0.33		

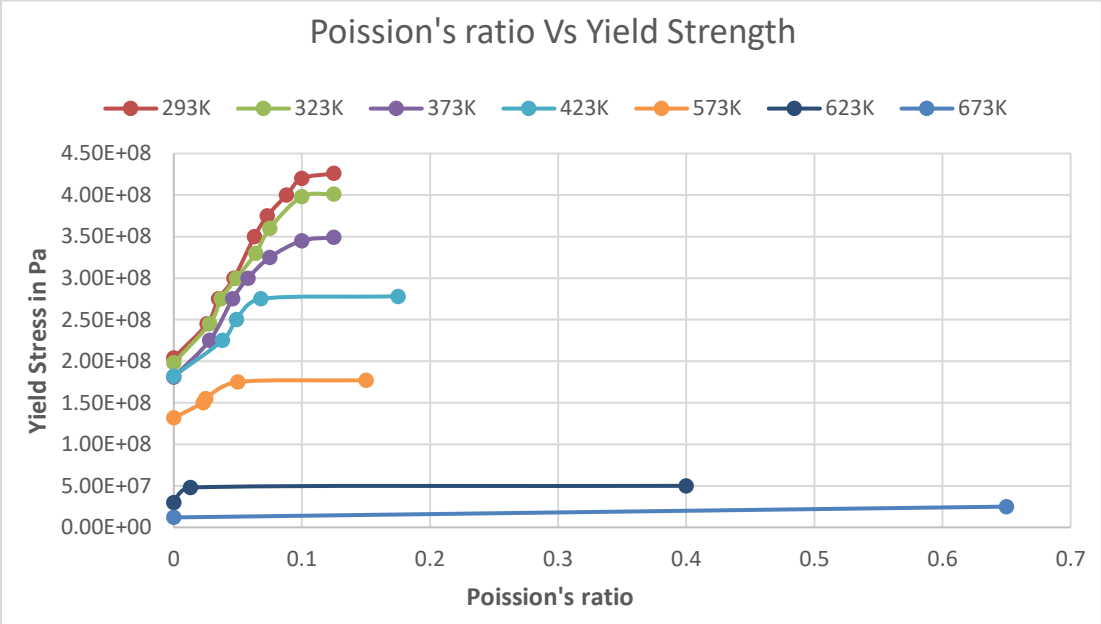

Figure 5.1: Plasticity

Table 5.2: Density Latent Heat, solidus and liquidous temperature

Density Kg/m^3	Latent Heat J	Solidus Temp K	Liquidus Temp K
2680	500000	830.15	870.15

5.1.2 DEFINING INITIAL, BOUNDARY CONDITIONS

Defining right initial and boundary conditions play a significant role in accurate simulation of stress and deflection in the digital model as they define the thermal and

mechanical constrains in specific to the physical print scenario. Initial conditions pertaining to this simulation are that initially the substrate is at room temperature of 300K or 26℃ and finally the substrate will be left to cool down to same temperature as initial. The mechanical boundary conditions used in this model are:

Step1: During printing process, the entire base plate is constrained, its movement along U1, U2, U3 is restrained in other words en-casterd(U1=U2=U3=0) as shown in Figure 5.2, physical model as in Figure 5.1 surface underneath the ears on either side are restrained with U3 movement or in ither words boundary condition of U3=0.

Step2; After the print is complete, the encaster constraints defined during Step1 are deactivated, only the selected nodes at the center as shown in Figure 5.3 and the defined.

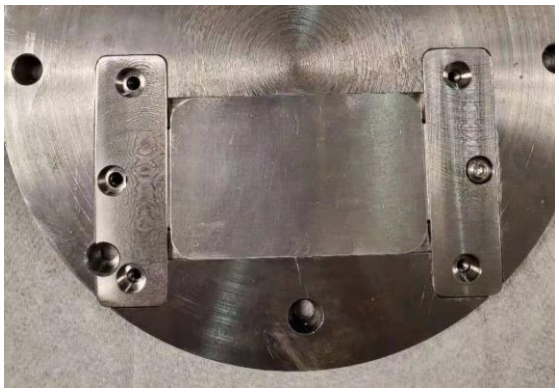

Figure5.2: Physical Model: Ears on rights and left U3=0

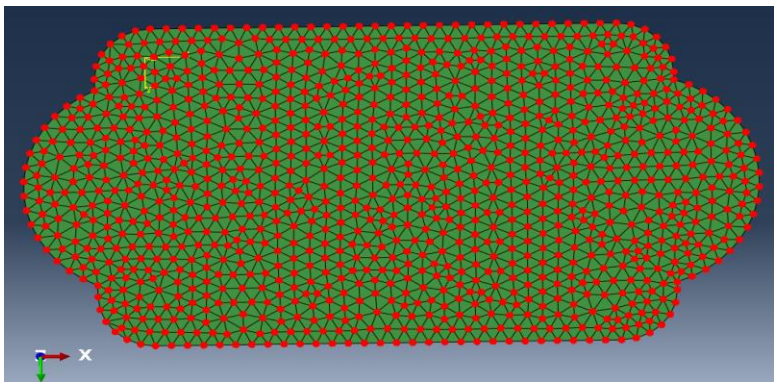

Figure5.3: Base nodes (U1=U2=U3=0)

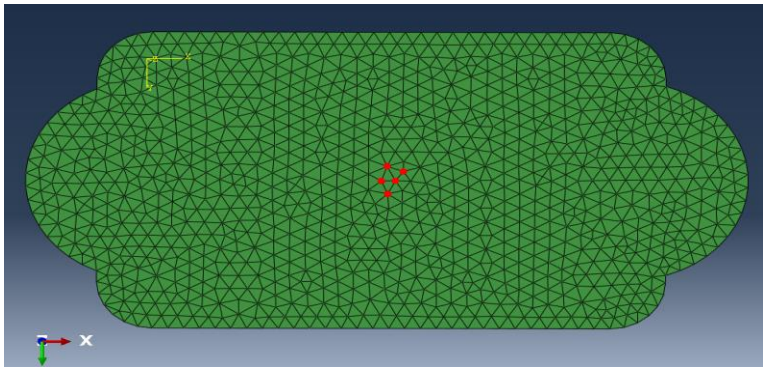

Figure: 5.4: Central nodes (U3=0)

5.1.3 PREDICTED DEFLECTION AND STRESS RESULTS

From the post processing of the successfully submitted model, we can extract U (deflection) and S (Stress) as shown in Figures 5.4, 5.5 respectively. The maximum deflection of 0.08mm is observed at the ears, the deflection is in the U-shaped bending inwards due to the compressive action of residual forces once the edge and bottom constrains are freed. The gradient of deflection is maximum at the edges and moving inwards it starts to fade and almost reaching to zero at the center of the plate.

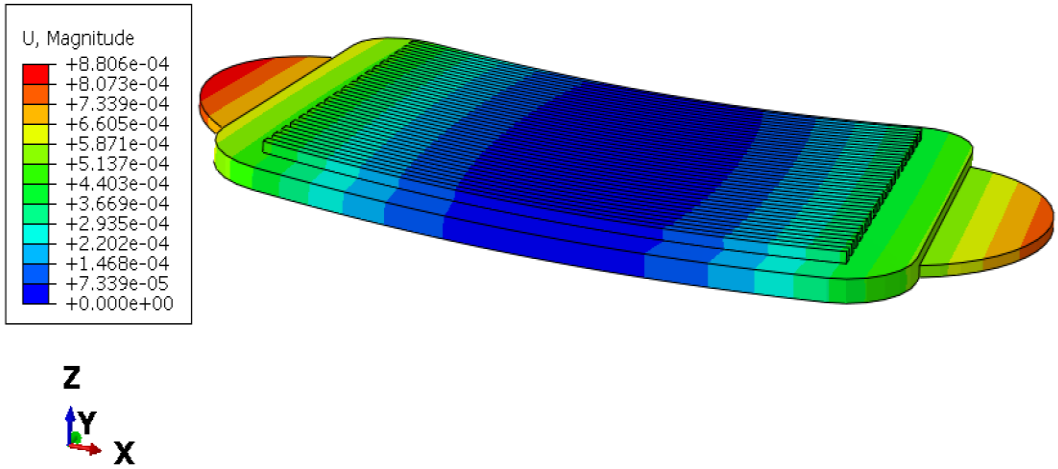

Figure 5.5: Deflection of Channel Plate

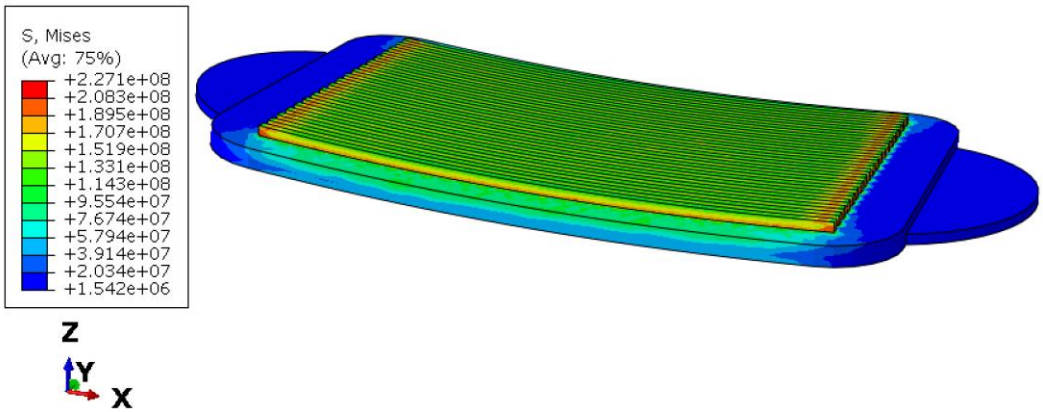

Figure 5.6 Stress profile a) Von Mises

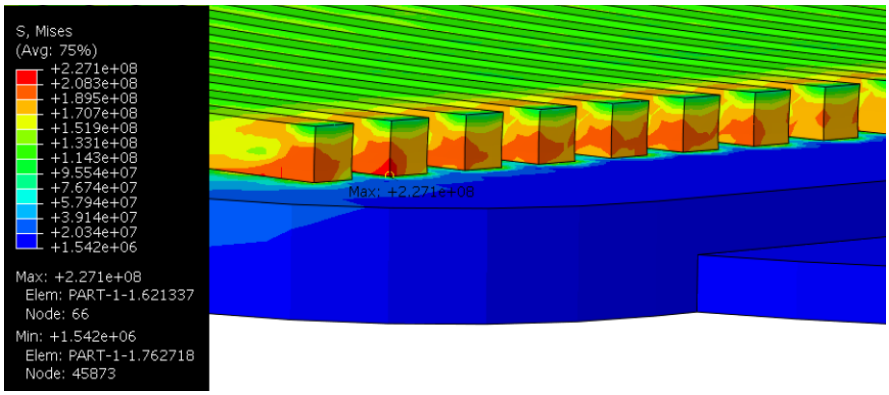

Figure5.6 b) Von Mises profile (detailed view)

The maximum stress of 227Mpa is seen at the starting and ending of the bars where their surface of contact with the substrate comes to an end. If this stress exceeds the local yield stress of material, warping or plastic deformation occurs. In Figure 5.5 we observe that the maximum stress is at the bottom most surface of the part, which is in contact with the substrate, obvious reason for the accumulated stress being the huge thermal gradient. The substrate is having larger surface area and can continuously dissipate heat and cool down, while with addition of every new layer, through conduction from the consecutive layers from above heat reaches the bottom most surface or 0^{th} layer of the part. Thus, once the part is let to cool down and detached from the substrate this accumulated stress leads to cracking.

5.2 DOG-BONE

A Dog-bone structure of dimensions 115 mm, 20 mm, and 3 mm in length, width, and height, respectively is selected for this study. It is manufactured by Fused Filament Fabrication (FFF) method. The part was built with PLA (Poly Lactic Acid; Plastic) as the filament, and for generating scanning strategy for printing NETFABB is used to generate the tool path and Python tool to generate Event Series form input G-codes.

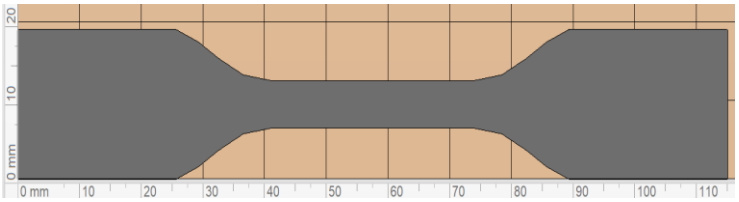

Figure 5.7: 2D view of dog-bone profile in NATFAB.

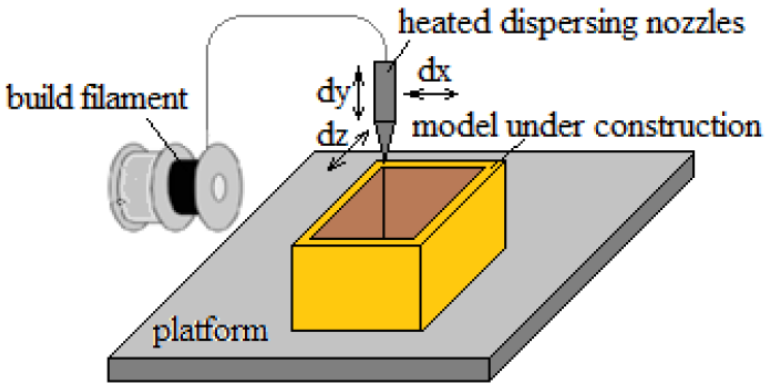

Figure: 5.8 Fused filament fabrication [34]

Material extrusion (ME) or also known as fused filament fabrication (FFF), is an additive manufacturing strategy whereby polymer filament is fed through a heated liquefier, is extruded through a nozzle, and is deposited on a build surface or previously printed layers where it quickly cools. Structural integrity of these AM parts is derived from bonding between adjacent and stacked extruded roads. Bonding forms via a polymer coalescence mechanism and is a function of thermal history at road interfaces. Which is

of a similar process as in metal AM process through LPBF if nozzle is replaced with a scanning laser of.

So, the Layer-wise model change method which is developed for LPBF can be widely applied to any process with similar mechanism of bonding between the stacked adjacent layers.

5.2.1 DEFINING MATERIAL PROPERTIES

The Dogbone is built with PLA material, the material properties are defined below in Table 5.3

Table 5.3: Material properties of PLA [35]

Density (kg/m^3)	1240
Specific Heat (J/kgK)	1800
Thermal Expansion (K^{-1})	4.1E-05
Conductivity (W/mK)	0.13
Tensile Modulus (MPa)	2.3E3
Ultimate Tensile Strength (MPa)	26.4
Tensile Strength at Yield (MPa)	35.9

5.2.2 DEFINING INITIAL, BOUNDARY CONDITIONS

Initial and boundary conditions they define the thermal and mechanical constrains in specific to the physical print scenario. Initial conditions pertaining to this simulation initially the substrate is at room temperature of 300K or 26℃ and finally the substrate will be left to cool down to same temperature. The mechanical boundary conditions used in this model are:

- During printing process, the entire base plate is constrained, its movement along U1,U2,U3 is restrained in other words encaster (U1=U2=U3=0), or in ither words boundary condition of U3=0.

5.2.3 TEMPERATURE PROFILES

In this case study one simulation result was derived from Model Chang method (Figure 5.9) and another is from PEA method (Figure5.10). To get the trend of temperature profile during printing, a specific node is selected at the center of the dog-bone marked with red node (in the Figures 5.9,5.10) and data of temperature Vs varying time and accumulating layer one on top of other, are plotted as in Figure5.11

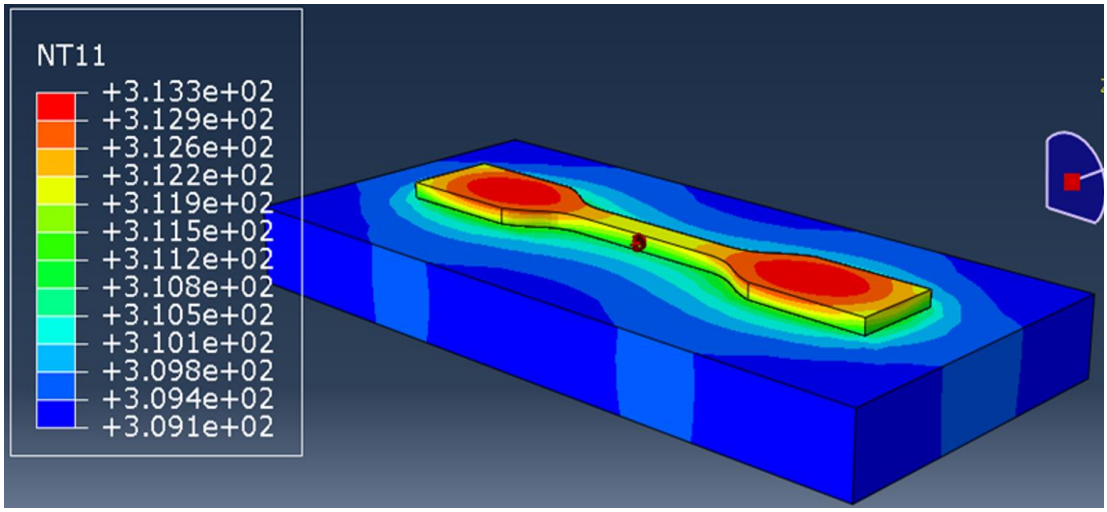

Figure 5.9: NT11 Model change method

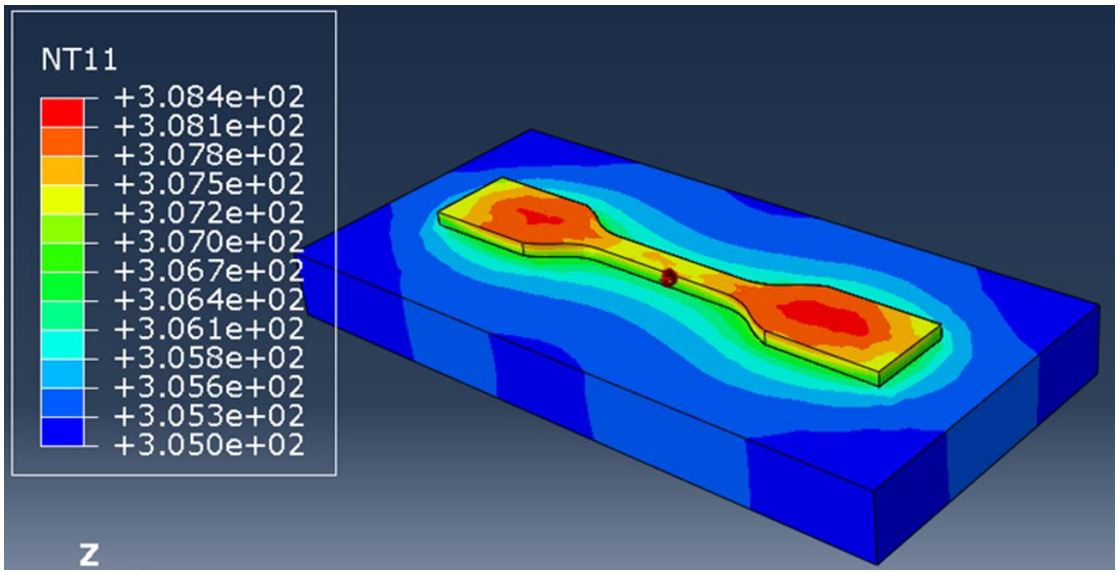

Figure 5.10: NT11 PEA method

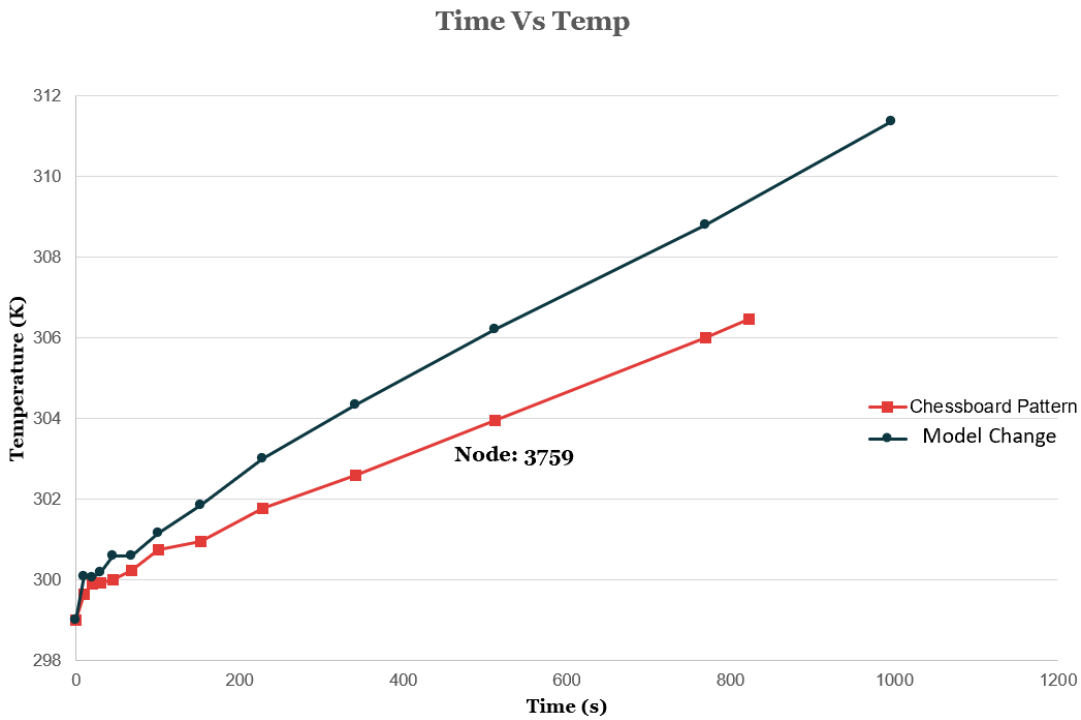

Figure 5.11: Temperature Vs Time Model change, PEA methods

AM process induces heat during the layer-by-layer addition process and Figure 5.11 represents the heat induced in printing. The time taken to complete the print by two different processes differ, as different activation strategies were followed in Layer-wise model change took 996 s and Progressive element activation method took 822 s for activation of 13 layers. The heat accumulation in Layer-Wise model change(LWMC) method is higher compared to PEA, since in LWMC the heat applied to each layer is calculated by Gaussian model[28] as discussed in section 3.1.1, while for PEA the heat is applied only at specific intersection that is selected from data in the Event-series files which are generated based on tool path and G-code files.

CHAPTER 6: CONCLUSION & FUTURE SCOPE

Firstly, two multiscale modeling approaches, Layer-wise model change method and Progressive elemental activation method have been tested against benchmark model. The Layer-wise model change method have been developed for efficient prediction of part distortion in LPBF. Simulation methodology and results for the two approaches have been compared. The key findings are as follows:

- Using the Layer-wise model change method, the thermo-coupled displacement model is used to calculate the deflections and the residual stress to predict part distortion. Using the Progressive elemental activation method separate thermal and mechanical analysis models were incorporated to predict part distortion.
- Similar deflection trends were found for both methods which also matched with the deflection trend of benchmark model. The progressive elemental activation method underestimated part deflection compared to the layer-wise model change method.
- The highest residual stress with a magnitude near the yield point of the work material was found on the top surface of the part. A typical residual stress profile along the depth direction for a LPBF part was predicted.

Secondly, a PBF printed channel plate of material Al10SiMg and a FFF printed dog-bone with PLA as material used design cases were studied with extended application of developed methodology for prediction of deflection and general temperature profile to predict and identify the possible regions where cracking might arise. The high stress

regions were found to be the top surface of the substrate and the bottom surface of the part. Thermal simulations also align with thermal gradient between the surfaces, thus the preheating the substate at the beginning of the process would reduce the thermal gradient and there by reduces the entrapped stress in the part.

However, there are further opportunities to develop the work as follows:

- Though the general trend of PEA matched with benchmark model, possible reasons for underprediction must be investigated. Possible factors for variation in results are suspected to be from accuracy of selection in the refinement of the mesh, size of the elements and temperature dependent specific material properties.
- To expand the capabilities of the residual stress prediction process through Model change method, future studies will focus on integrating scan patterns to Layer-wise activation to get more refined heat addition calculations which might reduce any over predictions. Which would also give closely accurate results with less computational resources.
- As we already can reasonably predict the residual stress and deflection from the in house developed layer-wise activation method, efficiency of this tool can further be optimized if it can integrate this data to predict the post-processing parameters like heating temperature, time and final unavoidable distortion in the printed part.

REFERENCES

[1] W. J. Sames, F. A. List, S. Pannala, R. R. Dehoff, and S. S. Babu, "The metallurgy and processing science of metal additive manufacturing," *Int. Mater. Rev.*, vol. 61, no. 5, pp. 315–360, 2016.

[2] L. N. Carter, C. Martin, P. J. Withers, and M. M. Attallah, "The influence of the laser scan strategy on grain structure and cracking behaviour in SLM powder-bed fabricated nickel superalloy," *J. Alloys Compd.*, vol. 615, pp. 338–347, 2014.

[3] H. Taheri, M. R. B. M. Shoaib, L. W. Koester, T. A. Bigelow, P. C. Collins, and L.J. Bond, "Powder-based additive manufacturing - a review of types of defects, generation mechanisms, detection, property evaluation and metrology," *Int. J. Addit. Subtractive Mater. Manuf.*, vol. 1, no. 2, p. 172, 2017.

[4] M. Markl and C. Körner, "Multiscale Modeling of Powder Bed-Based Additive Manufacturing," *Annu. Rev. Mater. Res.*, vol. 46, no. August, pp. 93–123, 2016.

[5] M. J. Matthews, G. Guss, S. A. Khairallah, A. M. Rubenchik, P. J. Depond, and W. E. King, "Denudation of metal powder layers in laser powder bed fusion processes," *Acta Mater.*, vol. 114, pp. 33–42, 2016.

[6] Y. Yang, J. Bin Lu, Z. Y. Luo, and D. Wang, "Accuracy and density optimization in directly fabricating customized orthodontic production by selective laser melting," *Rapid Prototyp. J.*, vol. 18, no. 6, pp. 482–489, 2012.

[7] W. J. Sames, F. A. List, S. Pannala, R. R. Dehoff, and S. S. Babu, "The metallurgy and processing science of metal additive manufacturing," *Int. Mater. Rev.*, vol. 61, no. 5, pp. 315–360, 2016.

[8] L. Mugwagwa, D. Dimitrov, S. Matope, and R. Muvunzi, "Residual stresses and distortions in selective laser melting - a review," *Int. Conf. Rapid Prod. Dev. Assoc. South Africa*, no. June, 2016.

[9] C. Li, Z. Y. Liu, X. Y. Fang, and Y. B. Guo, "Residual Stress in Metal Additive Manufacturing," *Procedia CIRP*, vol. 71, pp. 348–353, 2018.

[10] P. Mercelis and J. P. Kruth, "Residual stresses in selective laser sintering and selective laser melting," *Rapid Prototyp. J.*, vol. 12, no. 5, pp. 254–265, 2006.

[11] D. W. Brown, M. Kumar, G. F. Gallegos, and W. E. King, “An Experimental Investigation into Additive Manufacturing- Induced Residual Stresses in SS316LY. Yang, M. Allen, T. London, and V. Oancea, “Residual Strain Predictions for a Powder Bed Fusion Inconel 625 Single Cantilever Part,” *Integr. Mater. Manuf. Innov.*, vol. 8, no. 3, pp. 294–304, 2019.

[12] Z. Li, B. Li, P. Bai, B. Liu, and Y. Wang, “Research on the Thermal Behaviour of a Selectively Laser Melted Aluminium Alloy : Simulation,” 2018.

[13] T. Debroy *et al.*, “Progress in Materials Science Additive manufacturing of metallic components – Process , structure and properties,” vol. 92, pp. 112–224, 2018. L. N. Carter, M. M. Attallah, and R. C. Reed, “Laser powder bed fabrication of nickel-base superalloys: Influence of parameters; characterisation, quantification and mitigation of cracking,” *Proc. Int. Symp. Superalloys*, pp. 577–586, 2012.

[14] Q. C. Liu, J. Elambasseril, S. J. Sun, M. Leary, M. Brandt, and P. K. Sharp, “The effect of manufacturing defects on the fatigue behaviour of Ti-6Al-4V specimens fabricated using selective laser melting,” *Adv. Mater. Res.*, vol. 891–892, pp. 1519–1524, 2014.

[15] H. Gong, K. Rafi, H. Gu, G. D. Janaki Ram, T. Starr, and B. Stucker, “Influence of defects on mechanical properties of Ti-6Al-4V components produced by selective laser melting and electron beam melting,” *Mater. Des.*, vol. 86, pp. 545–554, 2015.

[16] D. Wang *et al.*, “The effect of a scanning strategy on the residual stress of 316L steel parts fabricated by selective laser melting (SLM),” *Materials (Basel).*, vol. 11, no. 10, 2018.

[17] K. Abd-Elghany and D. L. Bourell, “Property evaluation of 304L stainless steel fabricated by selective laser melting,” *Rapid Prototyp. J.*, vol. 18, no. 5, pp. 420–428, 2012.

[18] J. Karlsson, A. Snis, H. Engqvist, and J. Lausmaa, “Characterization and comparison of materials produced by Electron Beam Melting (EBM) of two different Ti-6Al-4V powder fractions,” *J. Mater. Process. Technol.*, vol. 213, no. 12, pp. 2109–2118, 2013.

[19] H. Ali, H. Ghadbeigi, and K. Mumtaz, “Effect of scanning strategies on residual stress and mechanical properties of Selective Laser Melted Ti6Al4V,” *Mater. Sci. Eng. A*, vol. 712, no. October 2017, pp. 175–187, 2018.

[20] C. Li, J. F. Liu, and Y. B. Guo, “Prediction of Residual Stress and Part Distortion in Selective Laser Melting,” *Procedia CIRP*, vol. 45, pp. 171–174, 2016.

[21] D. Hagedorn-Hansen, M. B. Bezuidenhout, D. M. Dimitrov, and G. A. Oosthuizen, “The effects of selective laser melting scan strategies on deviation of hybrid parts,” *South African J. Ind. Eng.*, vol. 28, no. 3SpecialEdition, pp. 200–212, 2017.

[22] P. Alvarez, J. Ecenarro, I. Setien, M. S. Sebastian, A. Echeverria, and L. Eciolaza, "Computationally efficient distortion prediction in Powder Bed Fusion Additive Manufacturing," *Int. J. Eng. Res. Sci.*, no. 10, pp. 39–46, 2016.

[23] D. Deng, S. Kiyoshima, K. Ogawa, N. Yanagida, and K. Saito, "Predicting welding residual stresses in a dissimilar metal girth welded pipe using 3D finite element model with a simplified heat source," *Nucl. Eng. Des.*, vol. 241, no. 1, pp. 46–54, 2011.

[24] M. Megahed, H. W. Mindt, N. N'Dri, H. Duan, and O. Desmaison, *Metal additive-manufacturing process and residual stress modeling*, vol. 5, no. 1. Integrating Materials and Manufacturing Innovation, 2016.

[25] A. J. Dunbar, E. R. Denlinger, M. F. Gouge, and P. Michaleris, "Experimental validation of finite element modeling for laser powder bed fusion deformation," *Addit. Manuf.*, vol. 12, pp. 108–120, 2016.

[26] K. Carpenter and A. Tabei, "On residual stress development, prevention, and compensation in metal additive manufacturing," *Materials (Basel).*, vol. 13, no. 2, 2020.

[27] N. Keller, A. W. Gmbh, and V. Ploshikhin, "New Method for fast predictions of residual stress and distortion of AM parts," no. April, 2015.

[28] L. Levine *et al.*, "Outcomes and Conclusions from the 2018 AM-Bench Measurements, Challenge Problems, Modeling Submissions, and Conference," *Integr. Mater. Manuf. Innov.*, vol. 9, no. 1, 2020.

[30] P. Mercelis and J. P. Kruth, "Residual stresses in selective laser sintering and selective laser melting," *Rapid Prototyp. J.*, vol. 12, no. 5, pp. 254–265, 2006.

[31] P. J. Withers and H. K. D. H. Bhadeshia, "Residual stress part 1 - Measurement techniques," *Mater. Sci. Technol.*, vol. 17, no. 4, pp. 355–365, 2001.

[32] https://www.nist.gov/ambench/chal-amb2018-01-pd

[33] Y. Yang, "Residual Strain Predictions for a Powder Bed Fusion Inconel 625 Single Cantilever Part," *Integr. Mater. Manuf. Innov.*, vol. 8, no. 3, pp. 294–304, 2019.

[34] A. I. Botean, "Thermal expansion coefficient determination of polylactic acid using digital image correlation," *E3S Web Conf.*, vol. 32, pp. 1–6, 2018.

[35] C. M. Dc, "Tecshnical data sheet," vol. 41, no. 0, pp. 2–4, 2014.